On the noise reduction of a porous trailing edge applied to an airfoil at lifting condition

Teruna, Christopher; Avallone, Francesco; Ragni, Daniele; Casalino, Damiano

DOI
10.1063/5.0047512

Publication date
2021

Document Version
Final published version

Published in
Physics of Fluids

Citation (APA)
Teruna, C., Avallone, F., Ragni, D., & Casalino, D. (2021). On the noise reduction of a porous trailing edge applied to an airfoil at lifting condition. *Physics of Fluids*, *33*(5), 1ENG. Article 055132. https://doi.org/10.1063/5.0047512

On the noise reduction of a porous trailing edge applied to an airfoil at lifting condition

Cite as: Phys. Fluids **33**, 055132 (2021); https://doi.org/10.1063/5.0047512
Submitted: 14 February 2021 . Accepted: 03 May 2021 . Published Online: 27 May 2021

Christopher Teruna, Francesco Avallone, Daniele Ragni, and Damiano Casalino

Physics of Fluids ARTICLE scitation.org/journal/phf

On the noise reduction of a porous trailing edge applied to an airfoil at lifting condition

Cite as: Phys. Fluids 33, 055132 (2021); doi: 10.1063/5.0047512
Submitted: 14 February 2021 · Accepted: 3 May 2021 ·
Published Online: 27 May 2021

Christopher Teruna,[a] Francesco Avallone, Daniele Ragni, and Damiano Casalino

AFFILIATIONS

Faculty of Aerospace Engineering, Delft University of Technology, Kluyverweg 1, Delft 2629HS, The Netherlands

Note: This paper is part of the Special Issue on the Lattice Boltzmann Method.
[a]**Author to whom correspondence should be addressed:** c.teruna@tudelft.nl

ABSTRACT

Numerical simulations, using a lattice-Boltzmann technique, have been carried out to study the effect of aerodynamic loading and Reynolds number on the aeroacoustics of a porous trailing-edge insert. The airfoil is a National Advisory Committee for Aeronautics 0018 with the last 20% of its chord being replaceable with porous insert based on a Ni-Cr-Al metal foam with a mean pore diameter of 0.8 mm. The porous insert is modeled as an equivalent fluid region governed by the Darcy's law. The angle-of-attack is set to 7.8°, and the freestream Reynolds numbers based on the airfoil chord are 2.7×10^5 and 5.4×10^5. The amount of noise reduction produced by the porous insert generally decreases as the angle-of-attack or Reynolds number is increased, although the far-field noise directivity remains similar to that of the solid insert case. Unlike for a solid insert, in which noise sources are concentrated at the trailing edge, those on the porous insert are distributed across the porous medium surface, and they promote phase interference effect that causes noise attenuation. This mechanism is realized by the pressure release process, which refers to the interaction between surface pressure fluctuations on both sides of the trailing edge through the porous medium. It is found that the pressure release process is strongly present at the last 25% of the porous insert extent, and thus the upstream segment plays a relatively limited role in noise attenuation. The porous insert also causes velocity deficit, enhanced Reynolds shear stress, and lower convection velocity in the turbulent boundary layer. Nevertheless, since only the flow field surrounding the porous insert is affected, the overall aerodynamic penalty is relatively minor. It has also been found that the effect of mean cross-flow inside the porous medium is almost negligible in the present investigation due to the small surface pressure difference between the two sides of the porous insert.

I. INTRODUCTION

Turbulent boundary-layer trailing-edge (TBL-TE) noise is one of the most common noise generation mechanisms in both aircrafts[1] and wind turbines.[2] This process is the result of pressure fluctuations in the TBL being scattered as acoustic waves when an abrupt change in surface boundary condition is present, such as a sharp trailing edge.[3] Considering that turbulent flows are common in industrial applications, various investigations have been performed to achieve TBL-TE noise mitigation, such as by performing airfoil shape optimization[4] and by applying TE addons, such as serrations[5–8] or permeable/porous TE inserts.[9–11]

Permeable TE inserts, in particular, have been demonstrated to be promising passive noise mitigation devices due to their ability to produce substantial noise reduction, with relatively small adverse aerodynamic impact.[12–15] These inserts tend to produce larger noise reduction when materials with higher permeability and porosity are employed, although this comes at the cost of aerodynamic penalty.[9] Nevertheless, it is necessary to understand the underlying principles of the porous inserts in order to better optimize their applications. A permeable TE insert is believed to enable a milder transition from the solid part of the airfoil to the freestream,[16,17] resulting in a weaker acoustic scattering at the TE.[3] However, it was later found that this process involves the interaction of pressure fluctuations between the upper and lower sides of the airfoil across the porous medium (PM),[18] which is referred to as the pressure release process. When this mechanism is hindered, for instance, by covering one side of the porous TE with non-permeable tape[17] or by introducing a solid partition inside the porous insert,[19] the noise attenuation capability of the porous TE completely disappears. Nevertheless, there are several aspects of the pressure release process that are still poorly understood, such as its relationship with the permeable TE geometry, material properties, and flow conditions. It is often necessary to observe the flow dynamics

inside the porous inserts to better understand them. Unfortunately, such measurements are often challenging to be performed experimentally,[20] and thus, high-fidelity numerical simulations often offer more flexibility in this regard.

Replicating porous media in simulations, however, can become quite costly, especially when considering materials whose pore size is much smaller compared to the overall dimension of the main body.[21] Several porous media modeling approaches have been proposed to overcome this challenge, such as by adjusting the wall boundary condition to include additional permeability and impedance characteristics.[22,23] In a different approach, referred to as the volume-averaging method, the internal volume of the porous medium is replaced by an equivalent fluid region, where additional physical conditions are imposed to take the porous media properties (e.g., permeability and porosity) into account.[11,24] This technique has been employed previously by the authors[14] for studying a National Advisory Committee for Aeronautics (NACA) 0018 equipped with a metal-foam TE insert, replicating the experimental setup of Rubio Carpio *et al.*[10] They concluded that, in addition to the smoother impedance transition at the TE, the destructive interference between the noise emitted by the distributed sound sources on the porous insert contributed toward noise attenuation.

This manuscript extends the authors' previous work[14] by investigating the porous TE aeroacoustics behaviors at a lifting condition and at different Reynolds numbers, which better represents the flow conditions that are often encountered in practice, such as on a wind turbine blade. Information gathered from the present investigation would also be useful to better understand the benefits and caveats of the current porous TE application. The rest of this manuscript is organized as follows. Section II provides a brief description of the porous material characterization and methodology, which includes the simulation setup and an overview of lattice-Boltzmann (LB) method in 3DS SIMULIA PowerFLOW^{TM}. Section III discusses on the effects of flow conditions on the aeroacoustic characteristics of the porous TE, while the aerodynamic aspects are examined in Sec. IV. The summary of this manuscript is provided in Sec. V.

II. METHODOLOGY

A. A brief description of the numerical technique

The commercial software 3DS Simulia PowerFLOW 5.4b based on lattice-Boltzmann (LB) method is used. The software solves the discrete Boltzmann equation for a finite number of directions. The LB method determines the macroscopic flow variables starting from the mesoscopic kinetic equation. The discretization used for this particular application consists of 19 discrete velocities in three dimensions (D3Q19), involving a third-order truncation of the Chapman–Enskog expansion.[25] The particle distribution function is solved on a Cartesian mesh, known as a lattice. An explicit time integration and a collision model are used, where the formulation based on a unique Galilean invariant is employed. Moreover, the equilibrium distribution of Maxwell–Boltzmann has been adopted.[25]

A very-large eddy simulation (VLES) model is implemented to take into account the effect of the sub-grid unresolved scales of turbulence. Following Yakhot and Orszag,[26] a two-equations $k-\varepsilon$ renormalization group is used to compute a turbulent relaxation time that is added to the viscous relaxation time. A wall model is used to approximate the no-slip boundary condition on solid walls, that is based on the extension of generalized law-of-the-wall model taking into account the effect of pressure gradient. These equations are solved iteratively from the first cell close to the wall in order to specify the boundary conditions of the turbulence model. For this purpose, a slip algorithm, obtained as the generalization of a bounce-back and specular reflection process, has been employed.

Far-field noise is computed using the Ffowcs-Williams and Hawkings (FW-H) analogy.[27] A forward-time solution[28] of the FW-H equation based on Farrasat's formulation 1A,[29] that is also extended for the application on a permeable surface, has been employed.

B. Simulation setup

The simulation setup is very similar to that described in Teruna *et al.*,[14] which replicates the experiment of Rubio Carpio *et al.*[10] It features a NACA 0018 airfoil, having a chord length of $c = 200$ mm and a span of $b = 80$ mm. The last 20% of the airfoil chord can be replaced with a porous TE, as shown in Fig. 1. The porous TE is modeled after a Ni-Cr-Al metal foam manufactured by *Alantum*. The properties of the metal foam has been obtained empirically,[19] and the relevant parameters are reported in Table I. Based on past experimental results, the porous insert made of metal foam with the mean pore diameter of $d_c = 800\ \mu$m offered the best trade-off between low-frequency noise attenuation and high-frequency excess noise,[10] and thus, this insert has been selected for the present study.

The porous insert is modeled using two layers of equivalent fluid regions. The APM (acoustic porous medium) model is applied at the outer layer, and PM (porous medium) model for the inner one. Both models are governed by the Darcy's law extended to include the Forchheimer's term. More details on the porous medium models can be found in Refs. 14 and 30. The APM layer follows the surface outline of the airfoil with a constant thickness of 1 mm, except at the last $0.005c$ of the airfoil chord where the local thickness is less than 1 mm. The PM region occupies the remaining volume underneath the APM layer. The multi-layer approach has been adopted to circumvent the need to specify the variation of resistivity (R_V and R_I) in the porous medium region depending on the thickness of the porous insert. This is achieved by isolating the outer layer, where the entrance effect

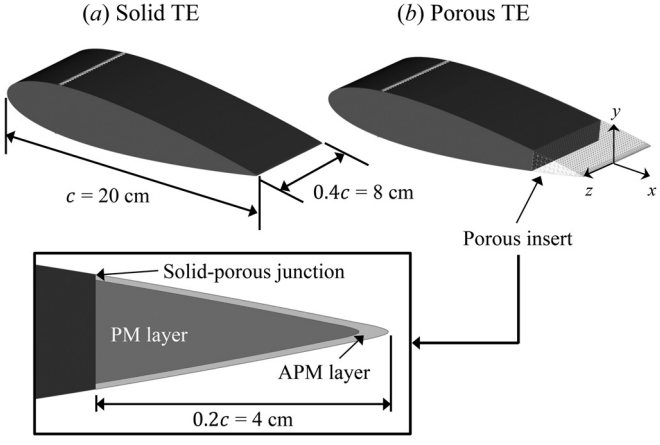

FIG. 1. The NACA 0018 with solid and porous TE. The inset shows the arrangement of multi-layer porous medium regions for porous TE cases.

TABLE I. The properties of Ni-Cr-Al metal-foam as reported by Rubio Caprio *et al.*[10] d_c—mean pore diameter; ϕ—porosity; K—permeability; C—form coefficient.

d_c (μm)	ϕ(%)	K (m^2)	C (m^{-1})
800	91.65	2.7×10^{-9}	2613

is strongly present, from the inner one that is dominated by the bulk effect.[31,32] To be specific, the entrance effect becomes more relevant as the porous medium thickness becomes comparable to the pore size, and it is mainly responsible for causing the overall resistivity value to vary with the porous medium thickness.[31] The porous medium region dominated by the entrance effect is referred to as the entrance length, which is approximately equal to the pore diameter for metal foams.[33] Underneath the entrance length, the bulk effect becomes more dominant, where the local resistivity no longer varies with porous medium thickness. The APM-PM combination has been verified in the past by the authors.[14]

Two freestream velocities have been chosen, $U_\infty = 20$ and 40 m/s, which correspond to chord-based Reynolds numbers of $Re_c = 2.7 \times 10^5$ and $Re_c = 5.4 \times 10^5$, respectively. The freestream approaches the airfoil that is installed at an angle-of-attack (AoA) of 7.8°, which has been chosen to realize a high-lift condition without causing flow separation near the trailing-edge region. In addition, the authors will also refer to their previous work[14] in which the airfoil is installed at zero AoA and $U_\infty = 20$ m/s, particularly where the effect of AoA is of interest. The list of the airfoil configurations and flow settings is shown in Table II.

To force boundary-layer transition, spanwise zigzag strips[34] have been installed on both sides of the airfoil at 20% of the chord length from the leading edge (LE). The zigzag trip height is $t_{trip} = 0.003c = 0.6$ mm, while the amplitude is $c_{trip} = 0.015c = 3$ mm and the wavelength is $\lambda_{trip} = 0.015c = 3$ mm. The tripping devices are the same as those in a previous investigation on a similar airfoil setup.[8] Although a different tripping technique was employed in the experiment,[19] it will be verified later that this does not significantly affect the acoustic characteristics of the airfoil in the frequency range where the noise attenuation caused by the porous TE is present.

The sketch of the computational domain is shown in Fig. 2. As indicated in Fig. 1, the origin of the coordinate system is the mid-span of the trailing edge. The x axis (streamwise direction) is aligned with the airfoil chord, the z axis with the airfoil span, and the y axis (vertical direction) is perpendicular to the others. Thus, the airfoil leading edge is located at $x/c = -1$ and the trailing edge at $x/c = 0$. A rectangular computation domain has been defined around the origin of the coordinate system, with the dimension of $100c$ in both x and y directions and b in the spanwise direction. Periodic boundary conditions are applied on the lateral faces of the simulation domain, while the other boundaries are specified as pressure and velocity inlet. Note that

TABLE II. List of airfoil configurations and flow settings.

Type	U_∞ (m/s)	Angle-of-attack (AoA)
Solid and porous TE	20	7.8° (present), 0° (Ref. 14)
Solid and porous TE	40	7.8° (present)

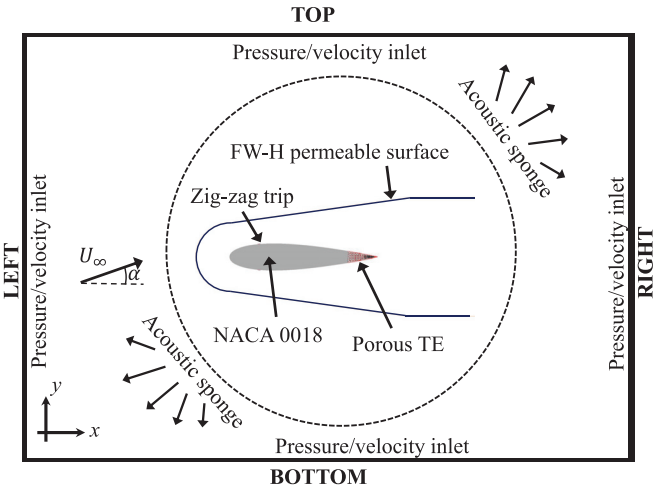

FIG. 2. A sketch of the computational domain. The domain boundaries are not drawn to scale.

PowerFLOW allows an inlet boundary to behave as a fluid outlet depending on the numerical solution. An acoustic sponge region is specified, starting from a radius of $36c$ from the origin, to mitigate acoustic reflection at the domain boundaries. The computational domain is divided into 10 grid refinement regions where local voxel dimension is allowed to vary by a factor of 2 between adjacent regions. The highest voxel resolution region is applied surrounding the airfoil surface. At the finest voxel resolution setting, the voxel size at the airfoil surface is $3.9 \times 10^4 c$, which guarantees that there are at least 10 grid points across the APM layer[30] of the porous trailing edge.

The discretization results in a total of 218×10^6 and 293×10^6 voxels inside the simulation domain for the solid and porous trailing edge cases, respectively. The simulation has been carried out for 20 flow passes, excluding the initial transient, during which pressure fluctuations on the surface and on the permeable FW-H surface are sampled at 75 kHz for far-field noise computations. The simulations have been run in the servers of Delft University of Technology with the porous TE case requiring a total of 38 400 CPU hours (i.e., processing time) on a 480-core Xeon Gold 6130 platform.

C. Grid independence study and validation

In this manuscript, grid independence study and validation are shown only for the 7.8° AoA cases, while the zero AoA ones can be found in Ref. 14. A grid independence study has been carried out using different resolution levels based on the number of voxels along the airfoil chord: 640 (coarse), 1280 (medium), and 2560 (fine). Hence, the grid refinement ratio is 2 between resolution levels and it is applied uniformly throughout the simulation domain. At the finest grid resolution level, the y^+ values at $x/c = -0.01$ for the solid TE case are 4.43 and 1.52 at the pressure side (PS) and suction side (SS), respectively, for $U_\infty = 40$ m/s, while for $U_\infty = 20$ m/s, they are 2.08 and 0.77, respectively. For the sake of brevity, only the results at the higher velocity are presented in several figures, especially since the variation of y^+ value with grid resolution setting is larger compared to that of the lower velocity case. Nevertheless, it has been verified that similar trends are found at $U_\infty = 20$ m/s.

In Fig. 3, the influence of the grid resolution settings on the mean surface pressure and skin friction coefficient is presented. Note that the discontinuity caused by the zigzag strip has been omitted from the plots and replaced with spline interpolation. The C_p distribution does not seem to be sensitive with respect to the different grid resolution levels. Discrepancies are more noticeable when comparing the C_f distribution, although this is expected since C_f values are based on the velocity gradient at the wall, which can only be accurately resolved with sufficiently fine wall-adjacent grid resolution. The figure shows that C_f plots for the medium and fine resolution settings produce a very good convergence behavior.

Since boundary layer quantities near the trailing edge are the most relevant for noise generation,[35,36] they are examined in Fig. 4. Without sufficient grid resolution, the mean velocity at the inner boundary layer region is generally overestimated compared to that at higher resolution, particularly at the pressure side where the boundary layer thickness is smaller. The simulation using the coarse grid also underestimates the turbulence intensity in the boundary layer, evidenced by the overall lower p_{RMS}. As mentioned in the authors' previous work,[14] the coarsest grid setting is insufficient to resolve the tripping mechanism of the zigzag strip. Following this, the fine grid setting is found to be sufficient for the rest of this investigation.

For validating the aerodynamic loading on the airfoil, the surface pressure distribution from the simulation is compared against that from the experiment[10] as shown in Fig. 5. The plots depict the pressure difference between the pressure side (PS) and suction side (SS) of the airfoil (i.e., $\Delta C_p = C_{p,PS} - C_{p,SS}$). It was observed in the experiment that the porous TE installation has negligible effects on the pressure distribution on the upstream part of the airfoil. This is indeed evident in the figure for both velocity cases. It is worth mentioning that the tripping device in the experiment is a double-sided tape with rough carborundum particles on it, unlike the zigzag strips in the simulation. While this has been previously shown to have minimal effect on

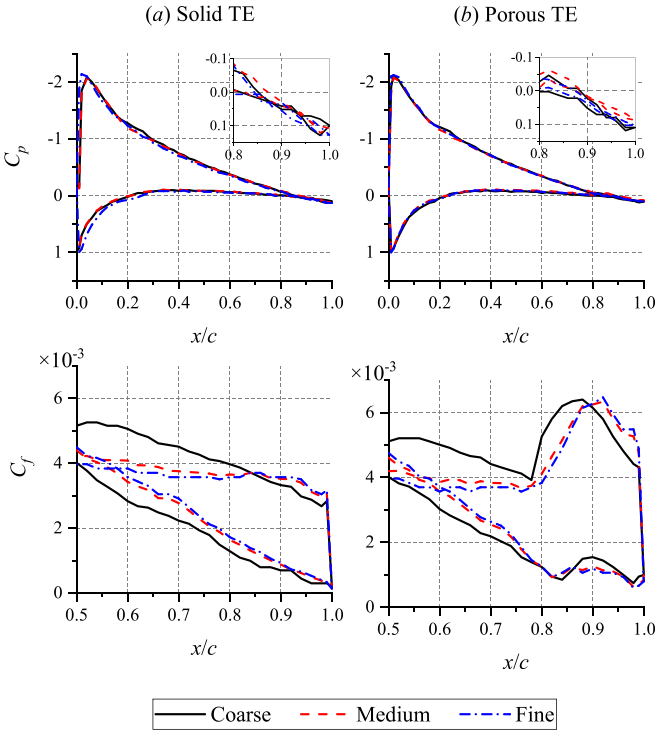

FIG. 3. The variation of the surface pressure distribution C_p (top row) and the friction C_f coefficients (bottom row) with grid resolution levels for $U_\infty = 40$ m/s and 7.8° AoA. The distributions for solid TE are shown under column (*a*) and porous TE ones under (*b*).

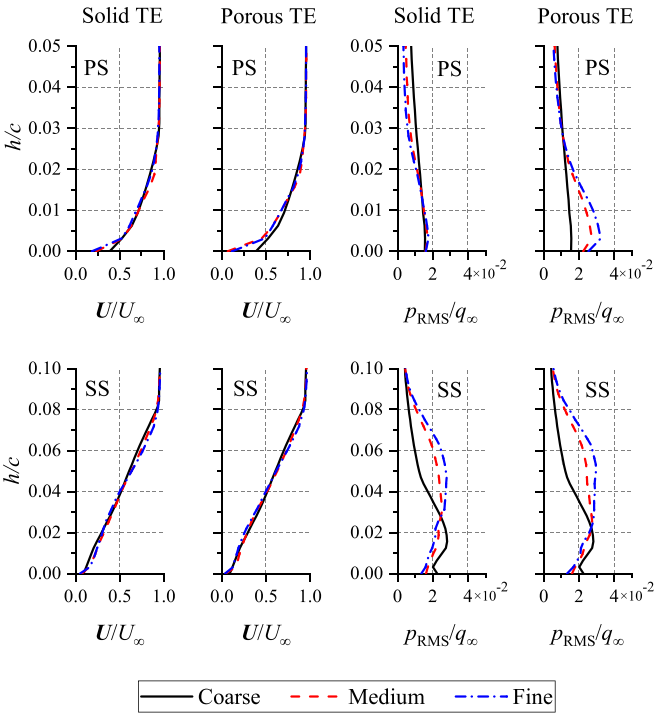

FIG. 4. Comparisons of velocity magnitude (***U***) and root mean square of pressure fluctuations (p_{RMS}) at different grid resolution levels. The values are shown for the 40 m/s cases at $x/c = 0.99$. PS: pressure side, SS: suction side.

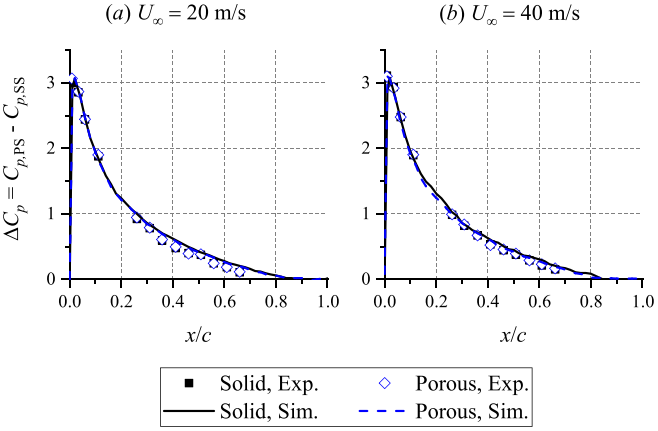

FIG. 5. The validation of the surface pressure difference ΔC_p between the pressure and suction sides of the airfoil at 7.8° AoA. Plot (a) shows the distribution for $U_\infty = 20$ m/s and (b) for $U_\infty = 40$ m/s.

acoustic scattering at the TE,[37] the difference might be responsible for the slight ΔC_p overestimation at $0.4 < x/c < 0.7$.

Far-field noise predictions based on the simulation are validated in Fig. 6. The noise spectra are shown in plots (a) for the solid TE and (b) for the porous one. Note that the frequency axis has been made non-dimensional as Strouhal number based on the airfoil chord ($St_c = fc/U_\infty$). The plots also compare the results obtained using either the surface FW-H approach or the permeable one. The figure shows that both the surface and permeable FW-H results for different TE types and velocities are almost identical in the frequency range of interest. This implies that the dipoles at the airfoil surface are the dominant type of noise sources. The spectra are then compared against those obtained from the experiment. The spectra for the solid TE case are generally in good agreement compared to the experiment. At lower velocity, however, the spectra from the simulation overpredict the experimental one above $St_c = 16$, which has been previously attributed to the self-noise from the zigzag trip.[14] The zigzag self-noise contribution is also apparent in the spectra for the porous TE case. The agreement between the experiment and the simulation results for the porous TE is slightly poorer, particularly at the low to mid frequency range. This discrepancy might be attributed to artifacts that could arise at the porous TE tip where the local porous material thickness is too small to be adequately represented by the APM layer. Nevertheless, the overall trend of the noise spectra is still captured by the simulation.

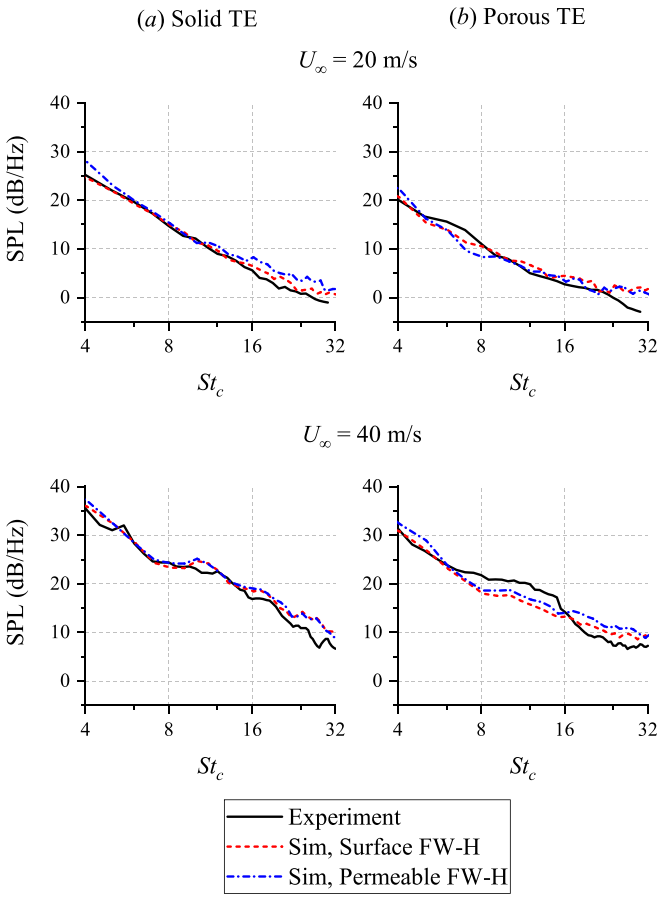

FIG. 6. Comparisons of far-field noise spectra obtained using different FW-H approaches against that from the experiment. The plots for solid TE are under column (a) and the porous TE ones are under (b). The observer location is $x/c = -0.68$, $y/c = 4.95$.

III. NOISE GENERATION FROM THE POROUS INSERT

A. Sound intensity and directivity

The far-field noise spectra and the noise reduction level produced by the porous TE are summarized in Fig. 7; column (*a*) depicts the effect of Reynolds number variation, and the angle-of-attack (AoA) effect is given in (*b*). In Fig. 7(a), the spectra at 20 m/s have been scaled following the U_∞^5 dependence of sound intensity produced by turbulence scattering at a TE[38] (e.g., the fifth power-law). To obtain the scaled sound pressure level ($\mathrm{SPL_{scaled}}$) from the original one ($\mathrm{SPL_{original}}$), the following formula is employed:

$$\mathrm{SPL_{scaled}} = \mathrm{SPL_{original}} + n \times 10 \log(U_{\infty,\mathrm{scaled}}/U_{\infty,\mathrm{original}}), \quad (1)$$

where n is the scaling exponent. The scaling of the sound spectra performs reasonably well for both solid and porous TE, although the discrepancies for the latter are more apparent at high frequencies. In column (*b*), it is revealed that the shape of the solid TE spectra varies with AoA. Nevertheless, the general shape of the porous TE spectra for any given AoA still resembles that of the solid TE. Considering that the TBL-TE noise can be linked to boundary layer parameters[36]

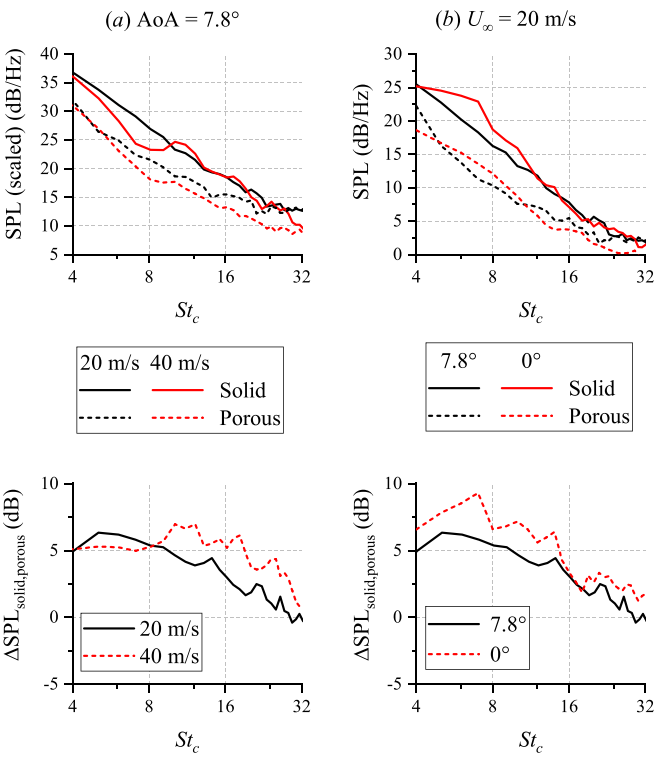

FIG. 7. The comparison of far-field noise spectra and noise reduction spectra for different TE types: (a) shows the Reynolds number effect at lifting condition, where the spectra at 20 m/s has been scaled to match that at 40 m/s following U_∞^5; (b) shows the AoA effect for $U_\infty = 20$ m/s.

on the airfoil (e.g., displacement thickness), the plot suggests that the porous TE does not cause significant alteration to the mean flow field but this will be further verified in subsequent sections. At 20 m/s and 7.8° AoA, the porous TE produces up to 6 dB of noise reduction at low frequencies ($St_c < 8$), which is smaller compared to the average noise reduction of 8.5 dB for zero AoA case. Increasing the velocity to 40 m/s, the noise reduction level reaches up to 7 dB in the mid frequency range ($8 < St_c < 16$). Nevertheless, it is evident that for both velocity cases, the noise attenuation level gradually becomes smaller as the frequency increases, which is also in line with the trends in analytical models.[39,40]

The noise attenuation capability of the porous TE is also reflected in the far-field noise directivity pattern, as shown in Fig. 8. The plots are arranged according to the chord-based Strouhal number with the

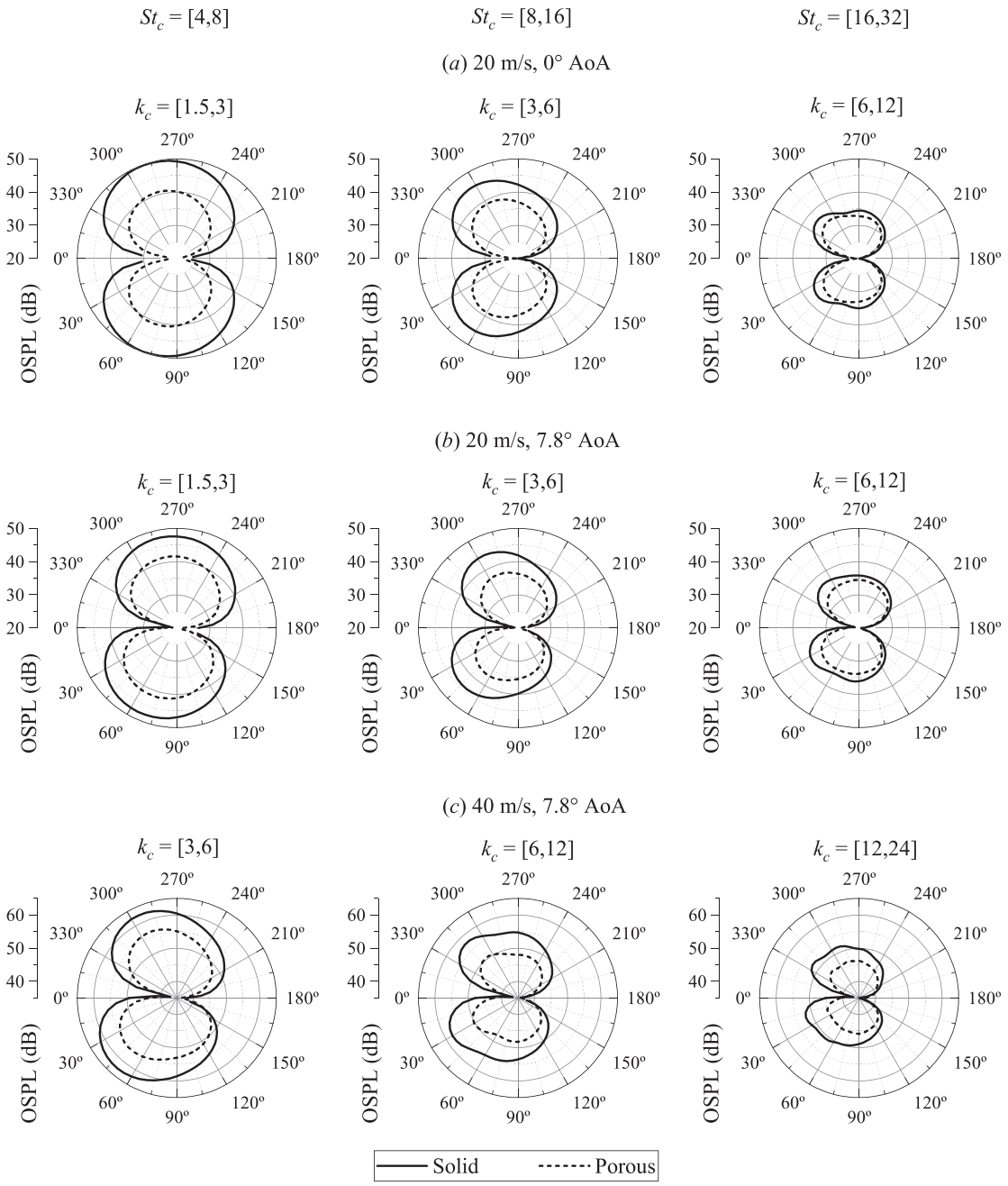

FIG. 8. Far-field noise directivity pattern at different velocity and AoA settings; 20 m/s, 0° AoA comparisons are in (a); 20 m/s, 7.8° AoA in (b); and 40 m/s, 7.8° AoA in (c). The freestream inflow comes from 0° toward 180°.

corresponding chord-based Helmholtz number ($k_c = 2\pi M_\infty St_c$) listed to indicate the acoustic-compactness of the airfoil at different frequency ranges. Comparing the plots under (a) and (b), it is apparent that changing the AoA causes the OSPL (overall sound pressure level) difference between the solid and porous TE to become smaller. The orientation of the main lobes is slightly tilted when the AoA is increased, but the general shapes of the lobes remain unaltered. For the Strouhal number range of $St_c = [4, 8]$ in Fig. 8(b), the solid TE at 20 m/s is still showing a dipole-like directivity given that the airfoil is acoustically compact ($k_c \sim 1$) in this frequency range. For the 40 m/s case, shown in Fig. 8(c), the sound directivity slightly resembles a cardioid shape since the Strouhal number corresponds to a higher Helmholtz number for which the airfoil is no longer compact. Non-compactness behavior becomes more prominent toward the high frequency range [$St_c = (16, 32)$] as multiple lobes can be identified in the sound directivity pattern. Nonetheless, increasing the Reynolds number does not appear to affect the tilt angle of the lobes. In general, the porous TE produces equal amount of noise attenuation toward both the upper and lower sides of the simulation domain, although a closer look reveals that the noise reduction level is relatively higher in the upstream direction, causing the directivity lobes of the porous TE to shift back toward the shape of a compact dipole. A similar trend has been observed for a perforated plate by Cavalieri *et al.*[40] and for a permeable slitted TE by Delfs *et al.*[18]

B. Sound source analysis

To further examine the sound source distribution on porous and solid TE, the airfoil is segmented into smaller regions whose far-field noise contributions are quantified. This analysis is based on the concept of partial-surface FW-H (PSFWH) integration. The reliability of the PSFWH approach relies on two conditions: (1) dipoles at the surface of a solid body are the only relevant noise sources in the system, and (2) sound propagation from the source to the observer location is unperturbed (e.g., there is no acoustic shielding from the environment surrounding the source region). These conditions have been verified in Fig. 10 where the spectra from the permeable FW-H approach have been found to be in good agreement with the surface FW-H ones.

In Fig. 9, it is shown that the airfoil planform has been divided into two main regions: the TE region that occupies the last 22% of the airfoil chord and the leading edge (LE) region that consists of $-1 < x/c < -0.22$. Hence, the airfoil with the porous TE has two locations where surface discontinuity is present. The one at $x/c = -0.22$ will be referred to as the "solid-porous junction," while the actual TE location ($x/c = 0$) is referred to as the "TE tip," in order to avoid confusion. The observer location for this analysis is the same as that for obtaining the noise spectra in Fig. 7 (i.e., $x/c = -0.68$, $y/c = 4.95$). The same technique has been employed by the authors to study the zero AoA cases in the past.[14]

Figure 10(a) compares the noise spectra produced by the entire airfoil surface with that from the TE region ($-0.22 < x/c < 0$), and it is clear that the latter dominates across the majority of the frequency range of interest. This plot confirms that the TE region is indeed the location where the dominant noise sources are present across the majority of the frequency range of interest. However, the TE contribution is noticeably lower than the total SPL at both the lower and higher ends of the spectra. At low frequencies, the noise from the airfoil also includes the contribution of the LE back-scattering[41] which becomes relevant when the airfoil is acoustically compact. On the other hand, the discrepancy in the very high frequency range can be associated with the self-noise contribution of the zigzag trip.[42] While the plot

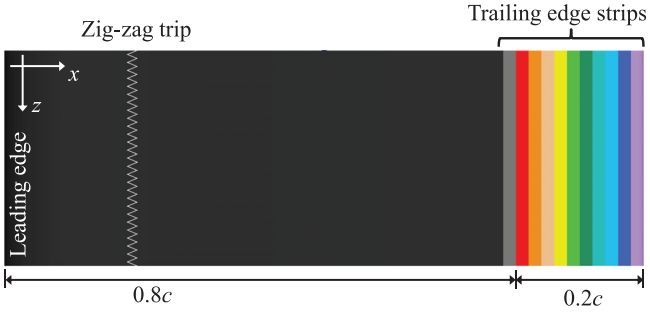

FIG. 9. The segmentation of the airfoil planform for far-field noise contribution analysis. The trailing edge strips cover the last 22% of the airfoil chord.

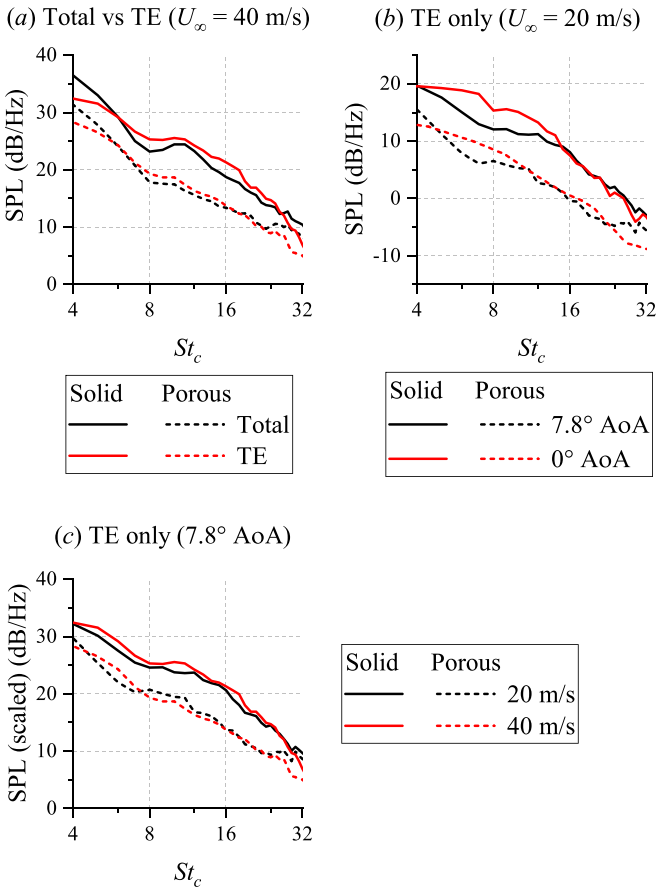

FIG. 10. (a) The comparison between the spectra of noise contribution from the TE region ($-0.22 < x/c < 0$) and the total ($-1 < x/c < 0$) at 40 m/s. The effects of AoA and Reynolds number on the noise contribution from the TE region are shown in (b) and (c), respectively. In (b), the SPL at 20 m/s has been scaled to 40 m/s following U_∞^5 for solid TE and $U_\infty^{5.7}$ for porous TE.

shows only the 40 m/s cases, the spectra at 20 m/s exhibit relatively similar behavior, although the effect of LE back-scattering can be found over a larger proportion of the low Strouhal number range given the lower Helmholtz number.

The spectra of the noise contribution from the TE region are shown in Figs. 10(b) and 10(c). The effect of AoA on the TE noise is depicted in plot (b). For the solid TE, discrepancies are present in the spectra between $4 < St_c < 16$, which is due to the frequency shift in the noise produced by the pressure (low frequency component) and suction sides (high frequency component) of the airfoil.[36] The same effect is also present in the porous TE case, which results in the convex shape of the spectra at $6 < St_c < 12$. From this plot, it can be inferred that the porous TE becomes slightly less efficient when the AoA is increased. It is possible that this behavior is related to the increased turbulence scales at the airfoil suction side at higher AoA, considering that a sufficiently large ratio between the porous TE chordwise extent and the streamwise turbulence length scales in the boundary layer is necessary to mitigate noise effectively.[13,43]

In Fig. 10(c), the spectra at 20 m/s have been scaled to 40 m/s following the acoustic intensity dependence[38,44] on freestream velocity. To produce the best fit, a U_∞^5 scaling is applied for the solid TE, and $U_\infty^{5.7}$ for the porous TE; similar fit has been found in the experiment of Carpio *et al.*[13] The higher scaling exponent for the porous TE has also been observed in analytical studies,[39] indicating that the porous TE has lower scattering efficiency compared to the solid one. As a consequence, it can be argued that the discrepancies in the scaled noise spectra of the porous TE in Fig. 7(a) are mainly due to the difference in the noise contribution from the airfoil main body. For instance, this can be attributed to LE back-scattering, which is more relevant for the lower velocity case since the airfoil chord remains acoustically compact (i.e., based on the condition[45] of $M_\infty St_c < 1$) up to $St_c = 17$ at 20 m/s but only up to $St_c = 8.5$ at 40 m/s.

It has been reported that the porous TE attenuates noise by modifying the phase relationship of the dipole sources that are distributed along its surface.[14] To study how this mechanism is affected by the different flow conditions, the TE region is divided further into 11 smaller areas (strips), each with the chordwise extent of $0.02c$ as shown in Fig. 9, and the noise contribution of each strip is quantified. It has been verified that using a larger number of strips does not alter the observed trends. Figure 11 shows the cumulative sum of the noise contribution of multiple strips starting from $x/c = 0$. The effect of Reynolds number is considered in (a), while the effect of AoA is shown in (b). The cumulative SPL plots allow for identifying the phase relation between one strip and the others.[14] For instance, a positive gradient indicates that the newly added strip is in-phase with respect to the sum of the previous ones, while an out-of-phase relationship would lead to a flat or negative gradient. In plot (a), where values at different velocities are compared, SPL values at 20 m/s have been scaled to 40 m/s following U_∞^5 and $U_\infty^{5.7}$ dependence for solid and porous TE, respectively.

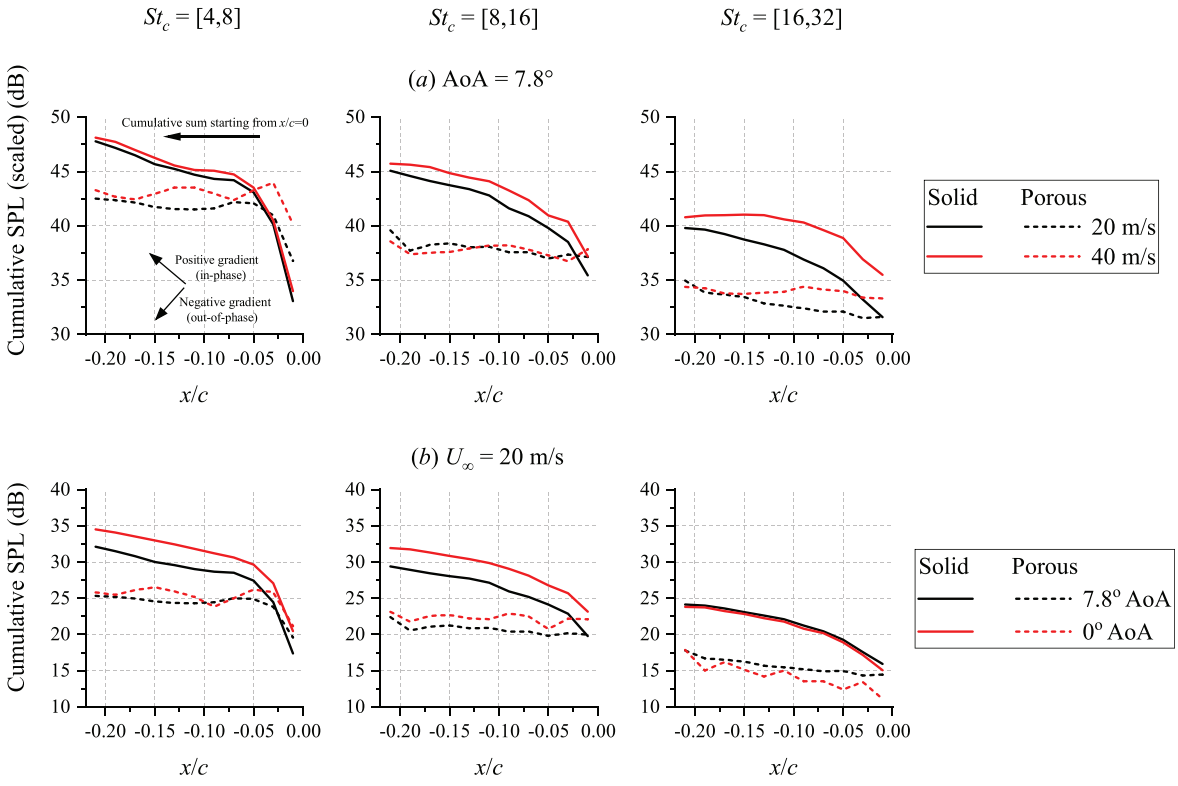

FIG. 11. The cumulative sum of sound pressure produced by each strip with a descending order (i.e., starting from the TE tip). In (a), the values at 20 m/s has been scaled to match that at 40 m/s following U_∞^5 for solid TE and $U_\infty^{5.7}$ for porous TE, respectively. The effect of AoA for the 20 m/s cases is shown in (b).

At the lowest Strouhal number range in Fig. 11(a), the cumulative SPL of the solid TE trends sharply upward until $x/c = -0.05$, which indicates that noise is mainly generated near the TE tip. Interestingly, the cumulative SPL values at $x/c = 0$ for the porous TE are higher than their solid counterpart, implying that the local source intensity at the TE tip is stronger for the porous TE. Further upstream, however, the cumulative SPL curves of the porous TE flatten out, unlike those of solid TE that still trend upward. This implies that the strips on the porous TE tend to be out-of-phase relative to each other, and the resulting phase interference between the different strips on the porous TE leads to noise reduction.[14] Although the cumulative SPL value of the porous TE at the TE tip ($x/c = 0$) is higher for the 40 m/s case, the difference at the solid-porous junction decreases to around 1 dB. This suggests that the phase interference effect on the porous TE surface also adapts with the different flow condition; the same behavior is also present at higher Strouhal number ranges. Nevertheless, the plot also suggests that the scattering at the TE tip of the porous TE tends to become more intense at higher Reynolds number as the cumulative SPL value near $x/c = 0$ for the 40 m/s case is higher than the one at 20 m/s. The effect of AoA is examined in Fig. 11(b). The plot shows that the cumulative SPL of the solid TE is shifted to a lower level at low and mid frequency ranges ($4 < St_c < 16$) for the higher AoA case, but the overall trends remain comparable. The same shift is also present for the porous TE cases, but with a much smaller proportion. As a result, the noise attenuation level of the porous TE becomes lower for the larger AoA case, although the phase interference effect is clearly present in the porous TE cases since their cumulative SPL curves tend to flatten further away from the TE tip.

Following Fig. 11, it is possible to conclude that the noise reduction mechanisms of the porous TE remain identical at different flow conditions, at least within the present range of AoA and Reynolds number. The metal-foam TE in the present investigation has a lower scattering efficiency compared to the solid one[11,19] due to the modification of phase relationships among noise sources at the porous medium surface; this mechanism has also been implied in several analytical studies.[40,46] The noise attenuation capability of the porous TE has been previously associated with the interaction between surface pressure fluctuations across the porous TE, which is referred to as the pressure release process.[18,19] It would be necessary to investigate the effects of Reynolds number and angle-of-attack on the flow field surrounding the porous TE to understand their implications on the acoustic characteristics that have been discussed in this section.

IV. FLOW FIELD DESCRIPTIONS

A. Boundary layer visualization and statistics

Vortical structures in the turbulent boundary layer can be visualized using the λ_2 criterion,[47] which allows for qualitative examination of the flow field. Figure 12 shows the instantaneous iso-surfaces of the λ_2 over the airfoil at 40 m/s and 7.8° AoA. Although they are not shown here, the iso-surfaces at 20 m/s exhibit similar behaviors. The figure clearly depicts the boundary layer transition process induced by the zigzag strips. Hairpin-like vortical structures can be observed in the wake of the zigzag strips. As these vortices travel past the mid-chord, they gradually evolve into flow structures that appear to be elongated along the streamwise direction. Turbulence production is also more prominent on the suction side than the opposite as the adverse pressure gradient along the former is stronger. Nonetheless, the figure does not show any noticeable difference in the boundary layer transition process between solid and porous TE.

The effects of the porous TE on the turbulent boundary layer are examined more closely in Fig. 13. Two flow quantities are shown in each row: the time-averaged wall-parallel velocity component U and the root mean square value of the Reynolds stress $(uv)_{\mathrm{RMS}}$. The boundary layer profiles are taken at 3 locations: (1) upstream of the solid-porous junction ($x/c = -0.23$), (2) middle segment of the porous TE ($x/c = -0.13$), and (3) near the porous TE tip ($x/c = -0.03$). The vertical axes represent the normal distance away from the wall, with the positive and negative values correspond to those for suction and pressure sides of the airfoil, respectively. The boundary layer at the third location is also plotted in terms of wall dimensions in Fig. 14, in which $U^+ = U/U_\tau$ and $(uv)^+ = (uv)_{\mathrm{RMS}}/U_\tau^2$ where U_τ is the friction velocity. The friction velocity for the porous TE is different from the solid TE one as the former does not have a no-slip condition at the surface, but for the sake of comparison, U_τ for the solid TE case under each flow setting is also used for the porous TE case.

When the airfoil is at a lifting condition, the boundary layer grows at a faster rate along the suction side due to the stronger adverse pressure gradient, which also causes the mean velocity profile to inflect inward (i.e., flow deceleration) along the inner region of the boundary layer.[48] The same phenomenon is also evident in Fig. 14(a), where the log-law region at the suction side deviates from that of the zero AoA case, unlike the one at the pressure side where the pressure gradient is milder. In general, the U and $(uv)_{\mathrm{RMS}}$ profiles of the solid and porous TE are identical at locations upstream of the solid-porous junction (i.e., $x/c < -0.2$). This is in line with experimental observations that the porous TE only affects the flow field locally.[12] Further downstream, the porous insert introduces a mean velocity deficit along the inner part of the boundary layer, indicating an increased friction along the porous wall,[49] which is also evident in Fig. 3 previously. The velocity deficit is more prominent at the inner region of the boundary layer, particularly below $y^+ = 100$, while the wake layer is virtually undisturbed. These phenomena are also reflected in the enhanced peak intensity in the Reynolds stress profile. Looking at the $(uv)_{\mathrm{RMS}}$ profile of the porous TE at $x/c = -0.03$, the increase in Reynolds stress level becomes more prominent for the higher Reynolds number case as the location of the peak $(uv)_{\mathrm{RMS}}$ level is closer to the surface. Since the higher $(uv)_{\mathrm{RMS}}$ level also indicates the generation of stronger pressure fluctuations beneath the boundary layer,[50,51] this might be the reason for the higher noise source intensity on the porous TE compared to its solid counterpart (see the cumulative SPL values near $x/c = 0$ in Fig. 11). It is also possible to deduce that the influence of the porous TE on turbulent fluctuations in the boundary layer depends on the proximity of the turbulent eddies from the porous medium surface.

When an airfoil with a porous TE is installed at a lifting condition, the pressure difference between the suction and pressure sides at the TE region may cause a mean cross-flow that could affect the turbulent boundary layer. To verify this, flow information inside the porous medium region are shown in Fig. 15. Note that the velocity components are aligned with the freestream direction, and the corresponding coordinate system is shown underneath each contour. The figure evidence that a mean cross-flow is almost nonexistent inside the porous medium given that the mean vertical velocity V is relatively small (i.e., $|V| < 0.005U_\infty$). The same conclusion can be inferred from the C_p

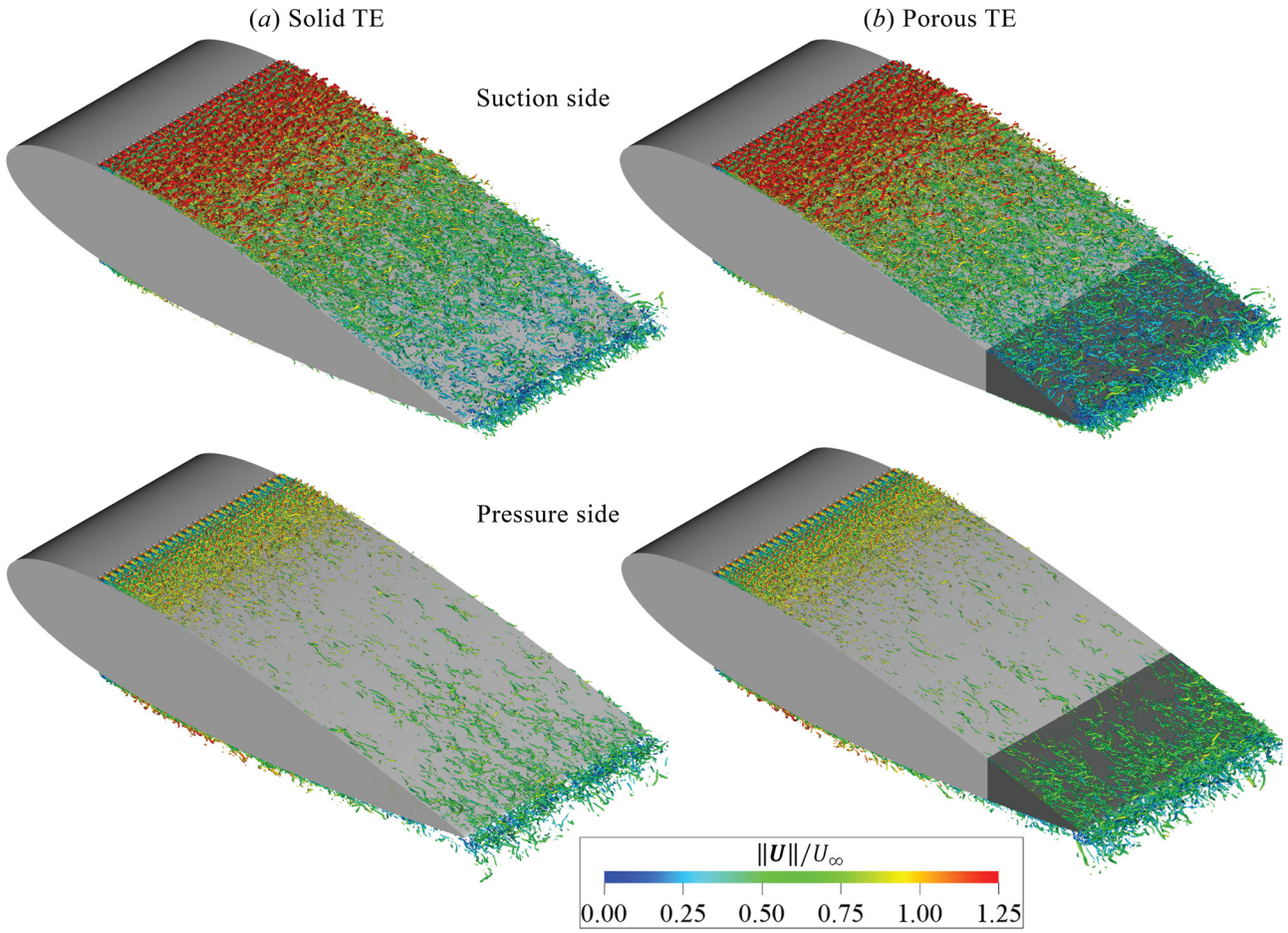

FIG. 12. Instantaneous iso-surface of $\lambda_2 = -4 \times 10^7 \mathrm{s}^{-2}$ at $U_\infty = 40$ m/s and 7.8° AoA, colored with the contour of non-dimensional velocity magnitude $\|\boldsymbol{U}\|/U_\infty$. The solid TE iso-surface is shown under column (a) and those for porous TE under (b).

contours, which shows that the static pressure variation in the vertical direction is smaller compared to that in the streamwise direction. This can be related to Fig. 5, where it has been depicted that the pressure difference between the opposite sides of the NACA 0018 airfoil is almost zero at the last 10% of the chord. The velocity vectors that are plotted on top of the mean streamwise velocity U contours show that the flow field mainly enters the porous medium at the downstream half of the TE, recirculates, and later exits near the solid-porous junction. Such recirculation tendency has also been found previously for the zero AoA case,[14] and it can be considered to be driven by the streamwise adverse pressure gradient that is shown in the C_p contours. As a consequence, this mechanism enhances the velocity gradient at the porous medium surface, and in turn, wall friction coefficient on the porous TE previously shown in Fig. 3.

Large velocity fluctuations (i.e., $v_{\mathrm{RMS}} > 0.01U_\infty$) inside the porous medium can still be found near the surface as depicted in the v_{RMS} contours. The v_{RMS} level also tends to increase toward the porous TE tip since the flow resistance is proportional with the local thickness of the porous medium. Higher v_{RMS} values can be found further into the porous medium at the pressure side, since the turbulent eddies are convected closer to the wall compared to those at the opposite side. This is particularly more apparent for the 40 m/s case due to the more significant enhancement of the Reynolds stress level as shown in Fig. 13. The Reynolds stress, which represents the momentum transport by turbulent motion, is initially higher on the suction side near the solid-porous junction. Toward the TE tip, however, the Reynolds stress level on the pressure side becomes comparable to that on the suction side, in addition to the location of the peak being closer to the porous medium surface. Therefore, the increase in $(uv)_{\mathrm{RMS}}$ on the porous TE is mainly the consequence of momentum transfer in the wall-normal direction at the porous medium interface.[52] Differently in the case of solid TE, the peak $(uv)_{\mathrm{RMS}}$ intensity at the pressure side remains lower compared to that at the suction side.

B. Pressure fluctuations characteristics

Considering that surface pressure fluctuations directly influence TBL-TE noise generation,[35,36,53] it is interesting to observe how they

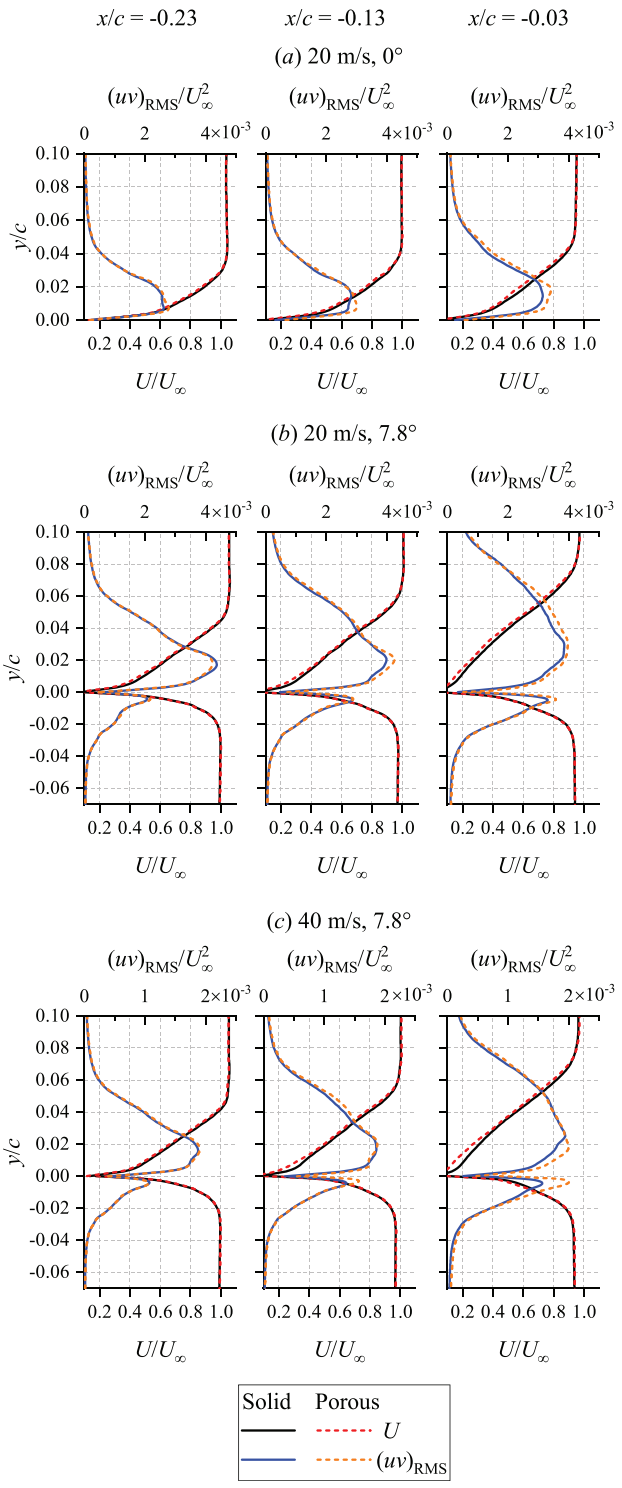

FIG. 13. Comparison of boundary layer profiles for solid and porous TE, depicting the mean wall-parallel velocity U and the root mean square of Reynolds stress $(uv)_{RMS}$. The profiles are plotted along the local wall-normal direction; 20 m/s, 0° AoA comparisons are in (a); 20 m/s, 7.8° AoA in (b); and 40 m/s, 7.8° AoA in (c).

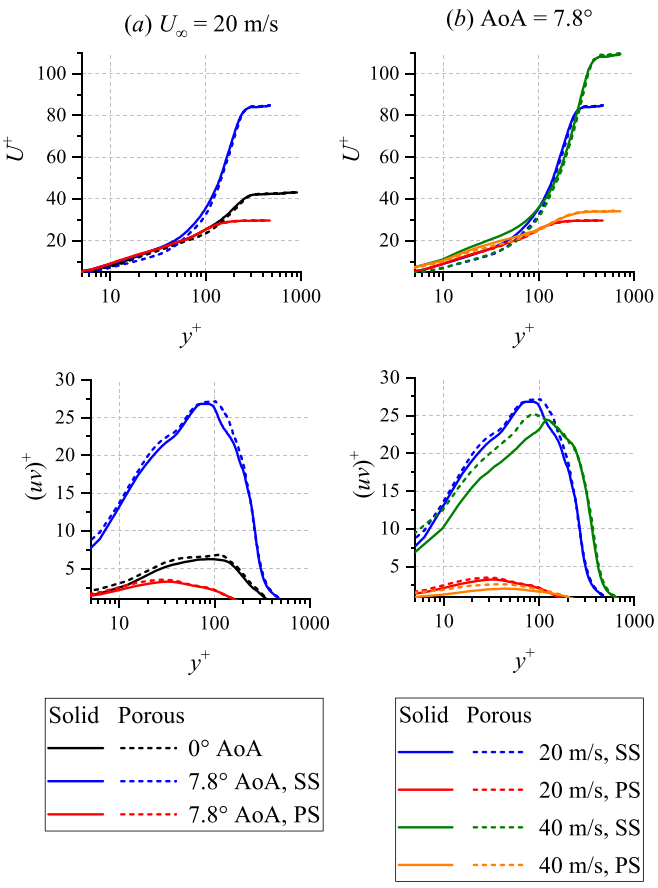

FIG. 14. U_∞ and $(uv)_{RMS}$ profiles at $x/c = -0.3$ plotted in non-dimensional form based on wall dimensions [U^+ and $(uv)^+$]. The plots depicting the AoA effect are in (a), and the Reynolds number ones in (b).

are affected by the porous TE. The surface pressure fluctuations spectra S_{pp} are presented in Figs. 16 and 17. Additionally for the porous TE, contours are plotted at several depth ratios y/d, where d equals to half of the local porous medium thickness. Thus, the porous TE surface corresponds to $y/d = 1$ and $y/d = 0$ is located along the chord line.

Figure 16 shows the pressure fluctuations spectra for the zero AoA cases. On the solid TE, pressure fluctuations increases toward the TE tip as the boundary layer grows. The S_{pp} level on the porous TE is relatively similar to the solid one upstream of the solid-porous junction ($0\,x/c < -0.2$), but it increases substantially further downstream. This is related to the enhanced $(uv)_{RMS}$ level as depicted in Fig. 13(a). When a positive AoA is applied in Fig. 17(a), the surface pressure fluctuations of the porous TE become more closely resembling that of the solid TE, although a more noticeable increase in S_{pp} level can be found along the pressure side. This is due to the pressure-carrying eddies, indicated by the peak $(uv)_{RMS}$ in Fig. 13, on the suction side being convected further away from the surface as the boundary layer approaches the TE tip. On the other hand, the peak $(uv)_{RMS}$ position on the pressure side does not vary substantially, despite the increasing Reynolds stress level as the boundary layer grows.

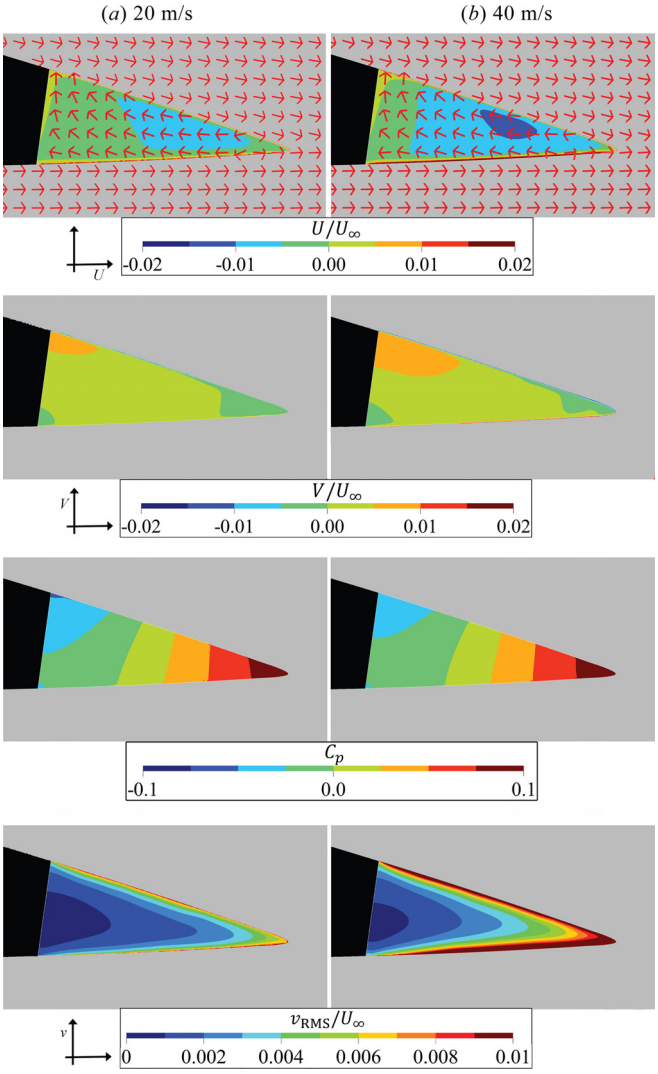

FIG. 15. The lateral view of the porous TE overlaid with contours of time-averaged streamwise and vertical velocity components (U and V, respectively), time-averaged pressure coefficient C_p, and the root mean square of vertical velocity fluctuations (v_{RMS}) inside the porous medium region at 7.8° AoA. Column (a) corresponds to $U_\infty = 20$ m/s, and (b) for $U_\infty = 40$ m/s. Mean velocity vectors are drawn as red arrows in the U contours, but their length is not to scale with the local velocity magnitude. External fluid region is masked in gray color.

Overall, the surface pressure fluctuations level is higher on the porous TE than on solid TE as a result of the stronger flow shear due to surface permeability. This can be considered the reason behind the higher cumulative SPL values of the porous TE near the TE tip ($x/c = 0$), particularly at low frequencies [see Fig. 11, $St_c = (4, 8)$]. However, the pressure fluctuations level drops significantly inside the porous TE. Averaged along the upstream half of the porous TE extent ($-0.2 < x/c < -0.1$), the S_{pp} level along the chord line of the porous TE is 12 dB lower than that at the surface. This difference decreases to around 5 dB at the last 4% of the airfoil chord where the local thickness is relatively small (e.g., approximately twice the pore diameter). Hence, there might be a limited segment of the porous TE where the pressure release process (i.e., the interaction of surface pressure fluctuations across the porous TE), which is responsible for noise mitigation,[18,19] can occur effectively.

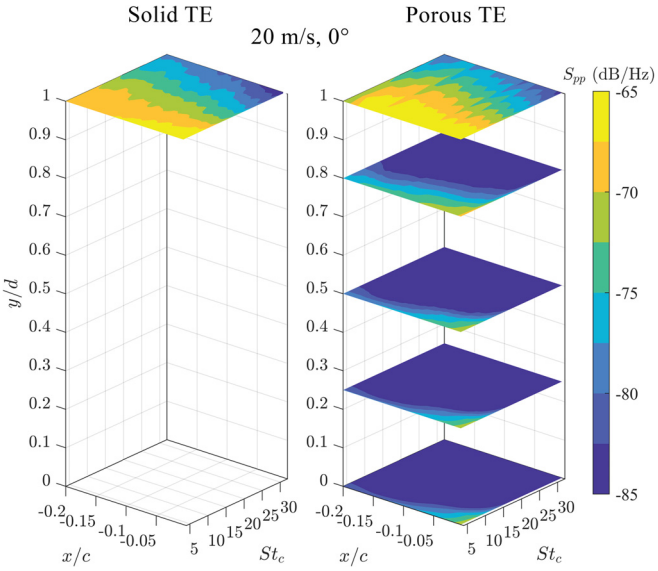

FIG. 16. Contours of spanwise-averaged pressure fluctuations spectra S_{pp} along the last 20% of the airfoil chord (0° AoA). For porous TE, the contours are plotted for different depth ratio y/d. S_{pp} has been normalized against freestream dynamic pressure q_∞^2.

In order to determine the chordwise extent in which the pressure release process can be found, a coherence analysis between the pressure fluctuations at the suction and pressure sides of the airfoil has been conducted, and the results are shown in Fig. 18. Pressure fluctuations are sampled at the airfoil surface for the solid TE, while for porous TE, they are sampled at the interface of the APM layer. The magnitude-squared coherence γ_{pp}^2 contours are shown on the left side, and the contours the phase angle A_{pp} in term of its cosine are given on the right side. γ_{pp}^2 is defined as follows:

$$\gamma_{pp}^2(f, \Delta x) = \frac{|C_{pp}(f, y_{ss}, y_{ps})|^2}{|C_{pp}(f, y_{ss}, y_{ss})||C_{pp}(f, y_{ps}, y_{ps})|}, \tag{2}$$

$$\begin{aligned} C(f, x, y_{ss}, y_{ps}) &= \int_0^T R(x, y_{ss}, y_{ps}, t) e^{-j\,2\pi f t}\, dt \\ &= |C(f, x, y_{ss}, y_{ps})| \left[\cos\left(A(f, x, y_{ss}, y_{ps})\right) \right. \\ &\quad \left. + j\,\sin\left(A(f, x, y_{ss}, y_{ps})\right)\right], \end{aligned} \tag{3}$$

where $C(f, x, y_{ss}, y_{ps})$ is the cross-power spectral density, at a given chordwise position x, of pressure fluctuations at the suction side y_{ss} and the pressure side y_{ps} of the airfoil. The cross-spectral phase angle is denoted as $A(f, x)$. j is equal to $\sqrt{-1}$. $\gamma^2(f, x)$ is computed using a periodogram method with Hanning window and 50% overlap, resulting in a frequency resolution of $\Delta f = 100$ Hz (i.e., $\Delta St_c = 1$ at 20 and $\Delta St_c = 0.5$ at 40 m/s).

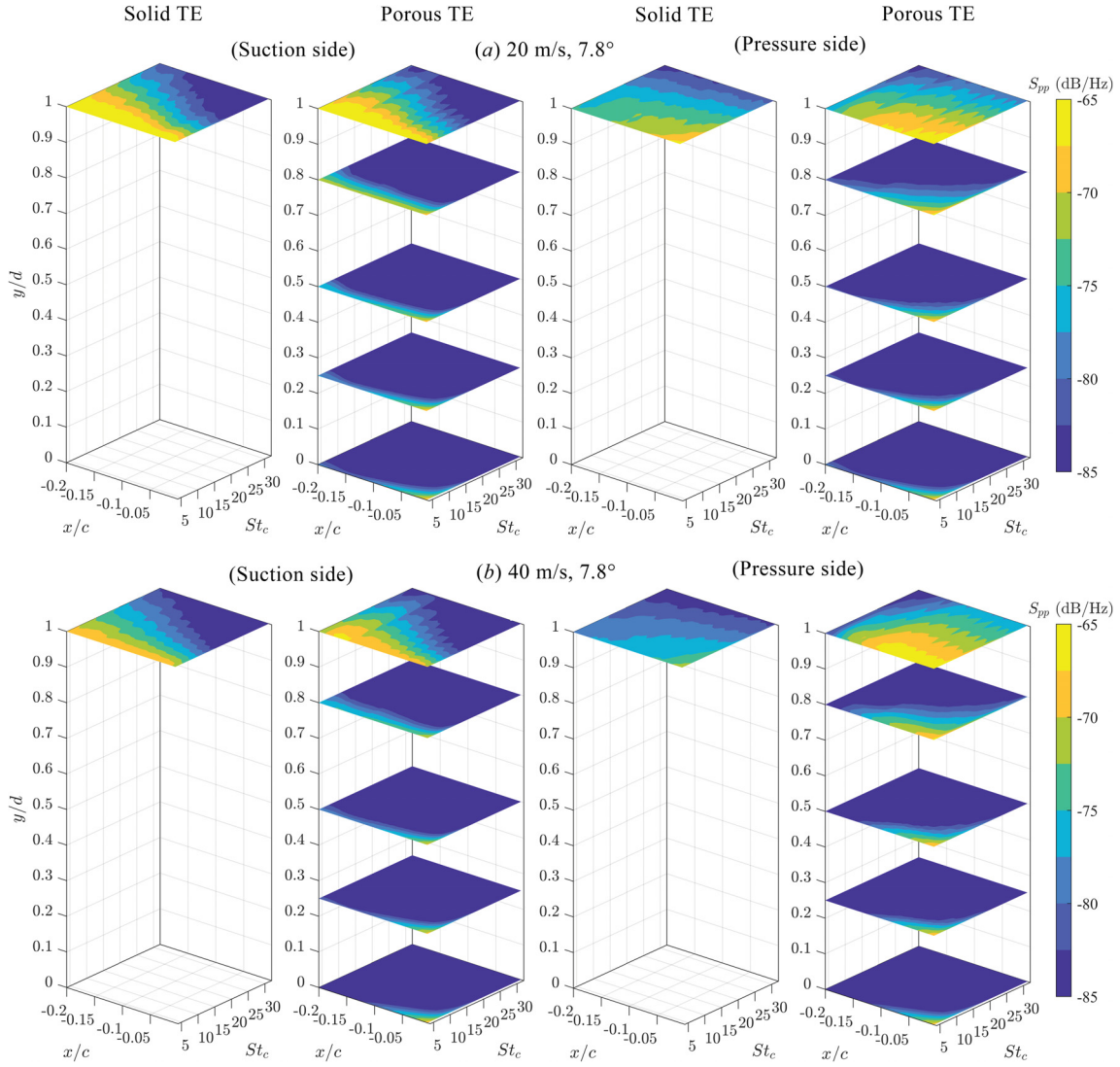

FIG. 17. Contours of spanwise-averaged pressure fluctuations spectra S_{pp} along the last 20% of the airfoil chord (7.8° AoA). For porous TE, the contours are plotted for different depth ratio y/d; for pressure side plots, the y/d direction is reversed. S_{pp} has been normalized against freestream dynamic pressure q_∞^2.

As expected, the impermeable surface of the solid TE prevents any coherence between pressure fluctuations on the opposite sides of the airfoil. On the other hand, the porous TE shows an increasing coherence level toward the TE tip, particularly at $x/c > -0.04$. This trend is also reflected in the $\cos(A_{pp})$ contours, where areas with higher coherence level also tend to have positive phase angle. As such, the pressure release process results in gradual phase equalization of the pressure fluctuations as they flow past the TE tip. Following the analytical model of Chase,[3] this mechanism would realize a milder acoustic scattering. The pressure release process is interpreted by the acoustic analogy as a modification of the phase relationship between the noise sources that are distributed along porous TE, which leads to the phase interference effect observed in the cumulative SPL plots (Fig. 11) earlier. Such mechanism is expected to be more effective for addressing the low frequency range where the airfoil is acoustically compact (i.e., when the dipole sources at the airfoil surface are strongly in-phase[44]), which could be a reason for the noise attenuation level of the porous TE being generally higher in the low frequency range.

Considering that a porous TE allows for a finite wall-normal velocity at its surface, the pressure release process can also be examined by performing a correlation analysis on the wall-normal velocity fluctuations,[19] which is shown in Fig. 19. In addition, the correlation curve is compared to the ratio between the pore diameter and the local airfoil thickness (d_c/h) to determine a link between the pressure release process and the TE geometry. The figure confirms that the pressure release process cannot take place in the solid TE. Conversely, the porous TE shows a dramatic increase in correlation level as the local TE thickness approaches the mean pore diameter of the metal-

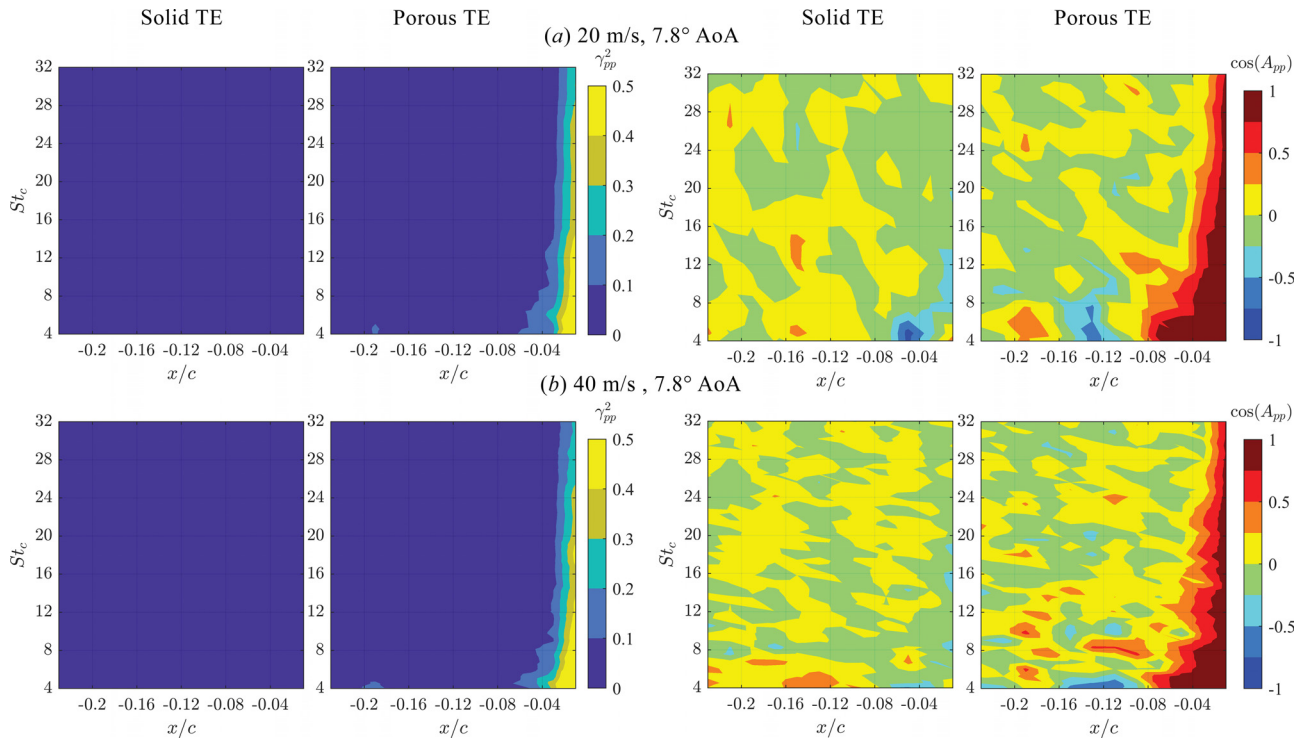

FIG. 18. The spatial distribution of magnitude-squared coherence of surface pressure fluctuations γ^2_{pp} at the airfoil surface and the corresponding phase angle A_{pp} between the suction and pressure side. The contours shown are for 7.8° AoA cases at $U_\infty = 20$ m/s (a) and $U_\infty = 40$ m/s (b).

foam. The correlation curves appear to be similar for the different Reynolds numbers and AoA settings. Hence, this suggests that the efficacy of the pressure release process depends mainly on the porous material properties and the TE geometry, at least within the present range of AoA and Reynolds numbers. Despite this, Figs. 7 and 10 suggest that the pressure release process is the most effective in the zero AoA case due to the turbulent boundary layers on both sides of the TE having similar characteristics.

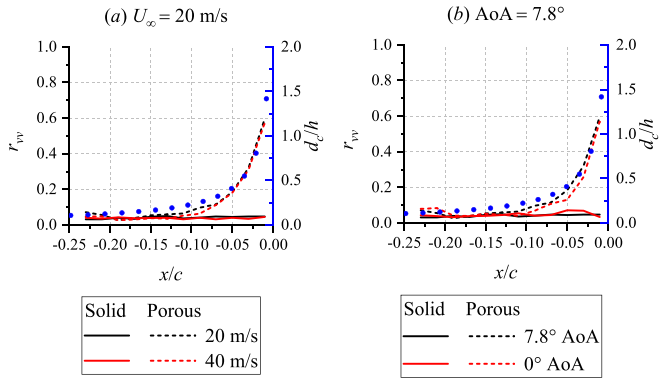

FIG. 19. The correlation coefficients of vertical velocity fluctuations r_{vv} between the suction and pressure sides of the airfoil. The secondary vertical axis (in blue) shows the ratio between the mean pore diameter of the metal-foam d_c and the local airfoil thickness h. The effect of AoA is shown in (a), and Reynolds number in (b).

Both Figs. 18 and 19 suggest the pressure release process takes place efficiently at the last 25% of the porous TE extent (i.e., 5% of the chord length), and consequently, the segment further upstream plays a relatively minor role in noise attenuation. This is consistent with recent observation of Carpio *et al.*[13] where a perforated TE insert with variable chord extent was tested on a NACA 0018 airfoil. As the porous extent was increased up to the last ≈5% of the airfoil chord, the noise attenuation level rose sharply. Further increasing the porous extent beyond ≈10% yielded almost no additional noise attenuation level. This trend has also been observed for other types of porous inserts with different permeability. As a practical consequence, it is conjectured that the application of the porous insert on an airfoil with a more slender shape near the TE tip would produce larger noise mitigation, provided that the incoming boundary layer properties are kept similar. However, this capability would be more susceptible to AoA variation as a porous medium with smaller thickness is less effective at preventing cross-flow between the opposite sides of the porous insert.

The pressure field beneath the boundary layer is mainly produced by eddies at convective wavenumber[50,54] that is proportional to f/U_c, where U_c is the convection velocity. Ananthan *et al.*[11] argued that the porous TE promotes a lower convection velocity that can be related to noise attenuation. To verify this, the convection velocity at the trailing edge region is computed using a space-time correlation of surface pressure fluctuations R_{pp} as follows:

$$R_{pp}(\Delta x, \Delta t) = \frac{\langle p(\boldsymbol{x}, t) p(\boldsymbol{x} + \Delta x, t + \Delta t) \rangle}{\sqrt{\langle p^2(\boldsymbol{x}, t) \rangle} \sqrt{\langle p^2(\boldsymbol{x} + \Delta x, t + \Delta t) \rangle}}, \quad (4)$$

where $p(\boldsymbol{x}, t)$ is the surface pressure fluctuations at a given location $\boldsymbol{x}$ and at time t, and Δx and Δt are the spatial and temporal separations, respectively. The contours of correlation coefficient are provided in Fig. 20 with the reference location at $x/c = -0.1$ (i.e., halfway between the solid-porous junction and the TE tip). The convection velocity U_c can be obtained by sampling maximum R_{pp} values at different Δx and Δt, such that $U_c = \Delta x/\Delta t$. The U_c is reported above each plot and it is represented as red dashed-line in the contour.

The figure evidences that the porous TE lowers the convection velocity in comparison with its solid counterpart, with larger discrepancies found at the pressure side. The boundary layer profiles in Fig. 13 can be used to interpret this observation. Since the dominant pressure-carrying eddies are found where $(uv)_{\mathrm{RMS}}$ is the highest,[50,51] the local streamwise velocity, where the $(uv)_{\mathrm{RMS}}$ peak is found in the boundary layer profile, would be equal to the convection velocity. In Figs. 13(b) and 13(c), the $(uv)_{\mathrm{RMS}}$ peak at the pressure side of the porous TE is generally located closer to the wall in comparison with that of the solid TE, implying a lower convection velocity. On the suction side, the shift in the $(uv)_{\mathrm{RMS}}$ peak location is less prominent, but the porous TE also introduces streamwise velocity deficit that also lowers the resulting U_c. Since the convection velocity on the porous TE is smaller than the solid TE one, the noise produced by the eddies is shifted to lower frequencies. Thus, for the porous TE, eddies that are responsible for noise generation for a particular frequency range are those of higher wavenumber that is generally weaker compared to its lower wavenumber counterpart. While this could contribute toward noise attenuation, the effect can be considered to be minor, since based on Fig. 10(c), a good fit between the spectra of solid and porous TE can be achieved only through shifting the frequency scale by more than 100%. On the contrary, the largest difference in U_c between the solid and porous TE in Fig. 20 is around 20%.

Following Amiet's model,[35] a reduction in the spanwise correlation length would result in noise attenuation, which could be the case for the porous TE. To verify this for the present cases, the spanwise correlation length of surface pressure fluctuations L_{pp}^z is computed as follows:

$$L_{pp}^z(f) = \lim_{\Delta z \to \infty} \int_0^{\Delta z} \sqrt{\gamma_{pp}^2(f, \Delta z)}\, \mathrm{d}z, \tag{5}$$

where γ_{pp}^2 is the magnitude-squared coherence of surface pressure fluctuations between a reference location and another that is separated by Δz along the spanwise direction. γ_{pp}^2 is computed using the same procedure as in Eq. (2). However, due to the limited simulation time, the correlation decay for $\Delta z \to \infty$ is not always achieved at low frequencies. As an alternative, the coherence function is fitted to an exponential function[55,56] as in the following:

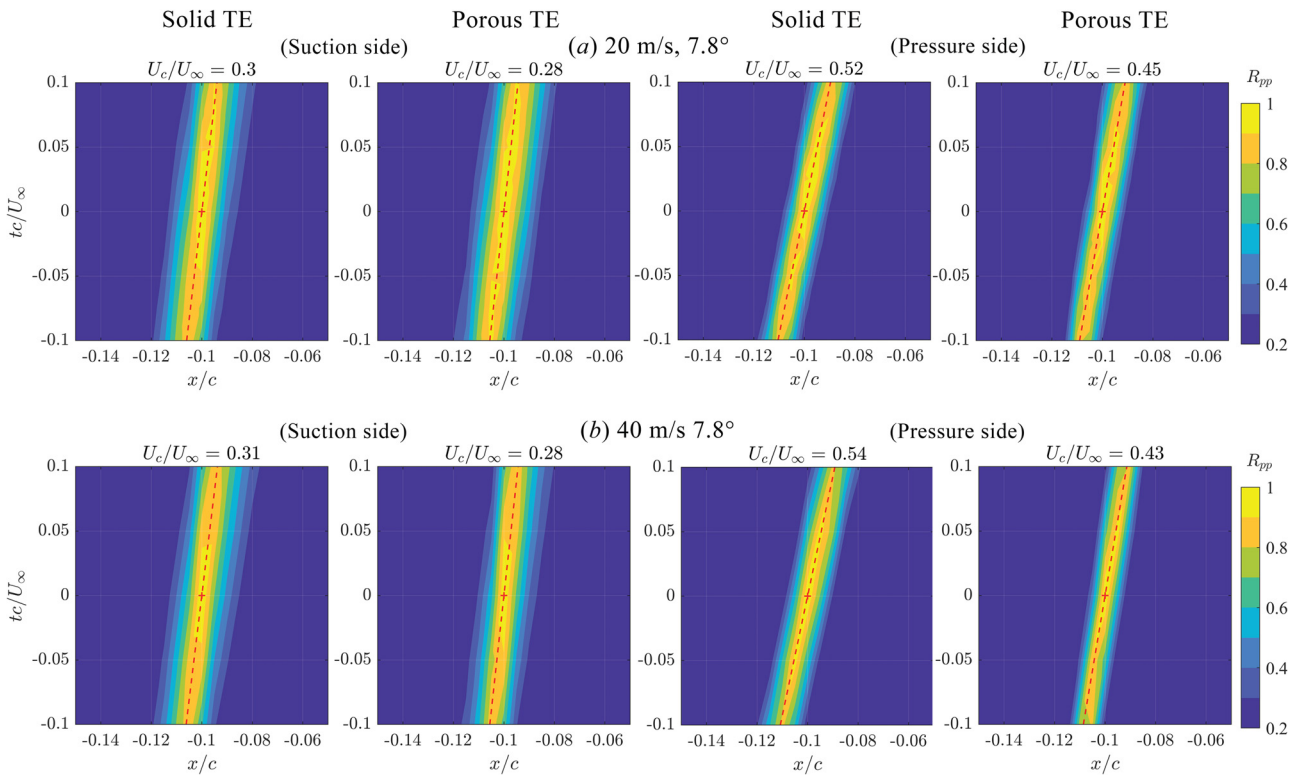

FIG. 20. Contours of spatiotemporal correlation coefficient of surface pressure fluctuations R_{pp} for the 7.8° AoA at $U_\infty = 20$ m/s (a) and $U_\infty = 40$ m/s (b). The reference location is at $x/c = -0.1$, marked by the red cross at the center of each contour. The gradient that corresponds to the convection velocity U_c is plotted as red dashed-line.

$$\gamma_{pp}(f, \Delta z) = e^{-\frac{|\Delta z|}{L^z_{pp}(f)}}. \tag{6}$$

L^z_{pp} values from Eq. (6) are averaged across 3 frequency bands as in Fig. 11. This procedure is repeated for 2 additional reference spanwise locations that are $0.05c$ apart from the TE midspan to obtain the spanwise-averaged results, which are shown in Fig. 21. In plot (a), the correlation length tends to increase toward the TE tip as the boundary layer becomes thicker. Interestingly for the porous TE, its L^z_{pp} values become smaller than the solid TE ones near $x/c = -0.1$, but both TE types show relatively similar correlation lengths near the TE tip. Increasing the AoA in plot (b), the L^z_{pp} values become larger, especially for the low frequency band $[St_c = (4, 8)]$. However, the difference between the solid and porous TE becomes less prominent at this inflow condition. Similar behaviors can be found for the higher Reynolds number case in plot (*c*). Thus, it is possible to conclude that the spanwise correlation length is not substantially affected by the presence of the porous TE, and it does not play a major role in noise attenuation.

C. Aerodynamic forces

Applying permeability on lifting bodies has been reported in literature[9,12,17] to lower aerodynamic performance. Following this, it would be interesting to quantify the impact of the metal-foam TE on the aerodynamic performance of the present NACA 0018 airfoil, particularly in regard to the lift reduction which has yet to be addressed in the authors' previous work.[14] The airfoil lift coefficient C_l is computed by integrating the time-averaged surface pressure coefficient C_p, previously shown in Figs. 3 and 5, along the airfoil surface as follows:

$$\begin{aligned} C_s &= \int_l C_p \cdot \boldsymbol{s}\, dl, \\ C_n &= \int_l C_p \cdot \boldsymbol{n}\, dl, \\ C_l &= C_n \cos(\alpha) - C_s \sin(\alpha), \end{aligned} \tag{7}$$

in which C_s and C_n are force coefficients in the tangential ($\boldsymbol{s}$) and normal ($\boldsymbol{n}$) direction relative to the chord line, respectively, while $\boldsymbol{l}$ is an infinitesimal segment of the airfoil surface curvature.

The airfoil drag is computed using a wake survey method,[57] which is described in the following:

$$C_d = 2\int_{-\infty}^{\infty} \left(1 - \frac{U(y)}{U_\infty}\right)\left(\frac{U(y)}{U_\infty}\right) dy, \tag{8}$$

where $U(y)$ is the time-averaged streamwise velocity component along the freestream-normal (y) direction. The limit of the integration is such that $U(y)$ is sampled in between $-2.5 < y/c < 2.5$, for a period of 10 flow passes. Subsequently, the drag coefficient is computed at different positions downstream of the airfoil to ensure that changing the wake survey position does not significantly affect the result. This is shown in Fig. 22, where the variation of C_d up to $x/c = 10$ has been presented. The plot shows that C_d is overestimated when the wake rake is close to the TE, but the value tends to converge at large x/c. The drag coefficients are subsequently averaged between $4 < x/c < 10$. Spanwise-averaging of both lift and drag coefficients is carried out to further improve statistical convergence.

The lift and drag coefficients of the airfoil are reported in Fig. 23. It is clear that the porous TE produces lower aerodynamic efficiency. Rounded to the nearest percentage, the lift reduction is almost 2%, while the drag increase is around 5%. Considering that the drag coefficient obtained from the simulation represents an optimistic prediction due to the neglected surface roughness effect, the porous TE appears to introduce more noticeable adverse impact on drag rather than lift. Nevertheless, it is likely that this trend depends on the airfoil profile and the flow incidence. For present configurations, the surface pressure difference across the porous TE is relatively small, and as a consequence, the airfoil lift is only affected slightly. The loss of lift could become more severe for an airfoil whose ΔC_p (pressure difference between the opposite sides of the airfoil) remains substantial near the TE region. This may be the case, for instance, with DU-96 airfoils which are widely used in wind-turbine aerodynamic studies.

V. CONCLUSION AND OUTLOOK

Numerical simulations using a lattice-Boltzmann solver, SIMULIA PowerFLOW™, have been performed on a NACA 0018 airfoil to investigate its turbulent boundary-layer trailing-edge (TE) noise. Noise mitigation is achieved by replacing the last 20% of the airfoil chord with a porous insert made of Ni-Cr-Al metal foam. The

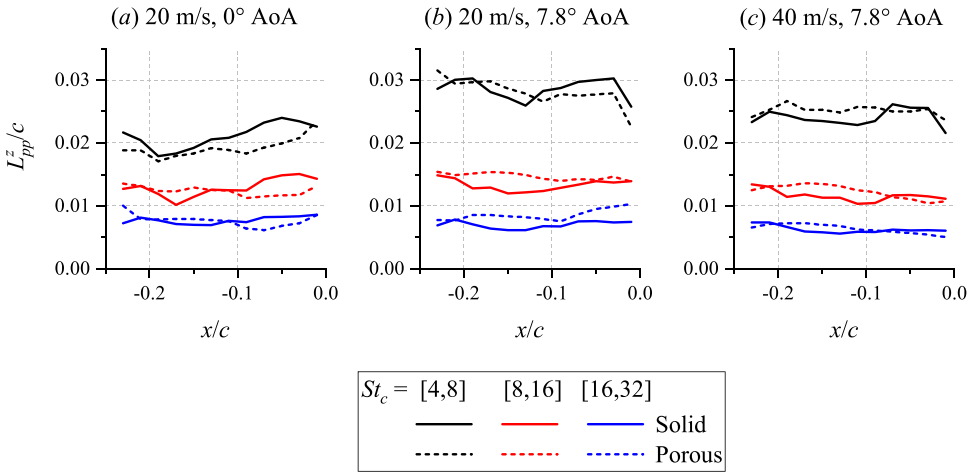

FIG. 21. Comparison of streamwise distribution of spanwise correlation length of surface pressure fluctuations L^z_{pp} between the solid and porous TE at different inflow conditions [20 m/s, 0° AoA in (a); 20 m/s, 7.8° AoA in (b); and 40 m/s, 7.8° AoA in (c)]. For plots (b) and (c), the values at the suction side are presented.

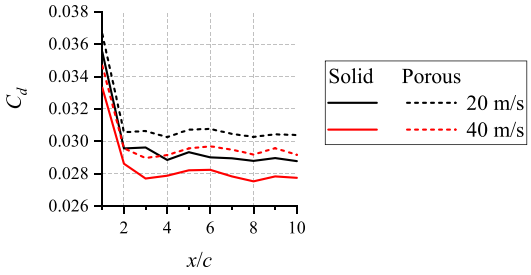

FIG. 22. The trend of C_d based on wake profile measured at different streamwise locations.

metal-foam properties are obtained empirically and supplied into a porous medium model based on Darcy's law in the simulation. The airfoil has a chord length of 0.2 m that is set to an angle-of-attack (AoA) of 7.8° and tested at freestream velocities of 20 and 40 m/s. Comparisons are also made against the zero AoA case at 20 m/s from the authors' previous work.

At lifting condition, the porous TE produces noise reduction of up to 7 dB, mainly in the low to mid frequency range; this is slightly smaller than the zero AoA at which a maximum noise reduction of 9 dB could be attained. By isolating the noise contribution from the TE region, it is observed that the noise intensity produced by the solid TE scales with the fifth-power to the freestream velocity (i.e., SPL $\propto U_\infty^5$), while a higher velocity exponent is applicable for the porous TE (SPL $\propto U_\infty^{5.7}$). However, this does not imply a transition in noise source type from a non-compact edge to a compact dipole, considering that the noise directivity pattern remains similar for both solid and porous TE. The TE region of the airfoil is divided into smaller strips to study the distribution of noise sources. While the noise sources are strongly in-phase relative to each other in the case of solid TE, they produce an opposite behavior on the porous TE, which promotes destructive interference and in turn, noise attenuation. Consequently, the acoustic scattering process on the porous TE becomes less efficient

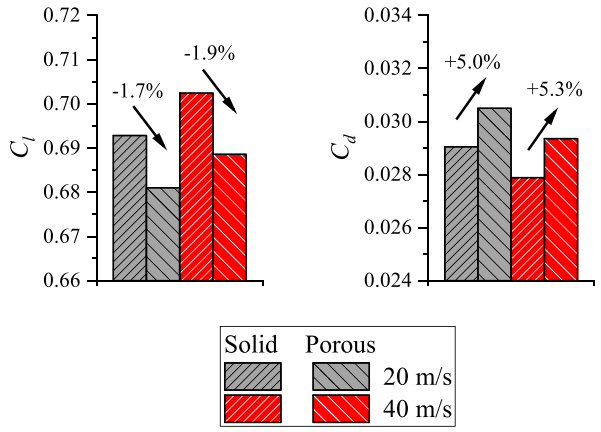

FIG. 23. The comparison of lift and drag coefficients between the airfoils with solid and porous TE. The percentage and the arrow above the bars indicate the difference between the coefficients for the porous TE relative to the solid TE.

than that on the solid TE. It has been found that the same noise reduction mechanism is present at the different AoA and Reynolds numbers considered in this study.

The porous TE also introduces several noticeable changes in the turbulent boundary layer, such as causing mean velocity deficit and enhancing Reynolds stress intensity. The latter is also indicative of higher flow shear near the porous medium surface and in turn, more intense surface pressure fluctuations. Since surface roughness effect is neglected in the simulation, these effects can be solely attributed to the permeability of the porous TE. It is also verified that no mean cross-flow is present across the porous TE despite the airfoil being in lifting condition. This is particularly due to the relatively small difference between the mean surface pressure on the suction and pressure sides of the airfoil. Instead, the mean flow field inside the porous medium forms recirculation regions. The present metal-foam TE also causes a slight aerodynamic penalty; the lift loss is found to be almost 2%, while the drag increase is around 5%.

The pressure release process, which is responsible for promoting noise attenuation, can be observed in the porous TE by performing coherence analysis of pressure fluctuations between the opposite sides of the airfoil surface. This mechanism becomes more prominent toward the thinner part of the porous TE, where it causes gradual phase equalization between pressure fluctuations on the suction and pressure sides of the airfoil. Since surface pressure fluctuations are related to the noise source characteristics, the pressure release process can be considered to modify the phase relationship among the noise sources on the porous TE surface relative to those on the solid TE, resulting in noise attenuation. This mechanism remains present at different freestream Reynolds numbers and angle-of-attack settings, although the largest noise reduction can be obtained when the flow fluctuations on both sides of the TE have similar spectral characteristics.

In line with the authors' past findings on a similar porous TE application, the present investigation suggests that the noise reduction of a porous TE cannot be attributed only to the changes in the flow field at the porous medium surface. Instead, the pressure balance process has to be taken into account in order to accurately predict the noise mitigation. As a consequence, simulations that consider the porous medium as a permeable–surface boundary condition would be unsuitable for porous TE studies. Nonetheless, it is interesting to observe that the present metal-foam insert is able to retain its noise mitigation capability at different flow conditions. However, the relationship between the porous material properties, TE insert shapes (which is determined by the airfoil profile), and the pressure release process still require further investigation. Furthermore, mathematical models that could relate the pressure release process with the noise attenuation level would be useful for obtaining optimization strategies in the future.

ACKNOWLEDGMENTS

This study was supported by the project SMARTANSWER (Smart Mitigation of flow-induced Acoustic Radiation and Transmission for reduced Aircraft, surface traNSport, Workplaces and wind enERgy noise), which has received funding from the European Union's Horizon 2020 research and innovation program under the Marie Skłodowska-Curie Grant Agreement No. 722401. More information can be found on https://www.h2020-smartanswer.eu/.

DATA AVAILABILITY

The data that support the findings of this study are available from the corresponding author upon reasonable request.

REFERENCES

[1]J. Revell, J. Revell, H. Kuntz, F. Balena, C. Horne, B. Storms, R. Dougherty, H. Kuntz, F. Balena, C. Horne *et al.*, "Trailing-edge flap noise reduction by porous acoustic treatment," in Proceedings of 3rd AIAA/CEAS Aeroacoustics Conference (1997), p. 1646.

[2]S. Oerlemans, P. Sijtsma, and B. M. López, "Location and quantification of noise sources on a wind turbine," J. Sound Vib. **299**, 869–883 (2007).

[3]D. M. Chase, "Noise radiated from an edge in turbulent flow," AIAA J. **13**, 1041–1047 (1975).

[4]A. L. Marsden, M. Wang, J. Dennis, and P. Moin, "Trailing-edge noise reduction using derivative-free optimization and large-eddy simulation," J. Fluid Mech. **572**, 13–36 (2007).

[5]S. Oerlemans, M. Fisher, T. Maeder, and K. Kögler, "Reduction of wind turbine noise using optimized airfoils and trailing-edge serrations," AIAA J. **47**, 1470–1481 (2009).

[6]L. Jones and R. Sandberg, "Acoustic and hydrodynamic analysis of the flow around an aerofoil with trailing-edge serrations," J. Fluid Mech. **706**, 295–322 (2012).

[7]T. P. Chong, A. Vathylakis, P. F. Joseph, and M. Gruber, "Self-noise produced by an airfoil with nonflat plate trailing-edge serrations," AIAA J. **51**, 2665–2677 (2013).

[8]F. Avallone, W. van der Velden, D. Ragni, and D. Casalino, "Noise reduction mechanisms of sawtooth and combed-sawtooth trailing-edge serrations," J. Fluid Mech. **848**, 560–591 (2018).

[9]T. F. Geyer and E. Sarradj, "Trailing edge noise of partially porous airfoils," in Proceedings of 20th AIAA/CEAS Aeroacoustics Conference (2014), p. 3039.

[10]A. Rubio Carpio, R. Merino Martinez, F. Avallone, D. Ragni, M. Snellen, and S. van der Zwaag, "Broadband trailing-edge noise reduction using permeable metal foams," in *Proceedings of INTER-NOISE and NOISE-CON Congress and Conference Proceedings* (Institute of Noise Control Engineering, 2017), Vol. 255, pp. 2755–2765.

[11]V. Ananthan, P. Bernicke, R. Akkermans, T. Hu, and P. Liu, "Effect of porous material on trailing edge sound sources of a lifting airfoil by zonal Overset-LES," J. Sound Vib. **480**, 115386 (2020).

[12]A. Rubio Carpio, R. M. Martínez, F. Avallone, D. Ragni, M. Snellen, and S. van der Zwaag, "Experimental characterization of the turbulent boundary layer over a porous trailing edge for noise abatement," J. Sound Vib. **443**, 537–558 (2019).

[13]A. R. Carpio, F. Avallone, D. Ragni, M. Snellen, and S. van der Zwaag, "Quantitative criteria to design optimal permeable trailing edges for noise abatement," J. Sound Vib. **485**, 115596 (2020).

[14]C. Teruna, F. Manegar, F. Avallone, D. Ragni, D. Casalino, and T. Carolus, "Noise reduction mechanisms of an open-cell metal-foam trailing edge," J. Fluid Mech. **898**, A18 (2020).

[15]K.-S. Rossignol, A. Suryadi, M. Herr, J. Schmidt, and J. Tychsen, "Experimental investigation of porous materials for trailing-edge noise reduction," Int. J. Aeroacoustics **19**, 365–384 (2020).

[16]R. E. Hayden, "Fundamental aspects of noise reduction from powered-lift devices," SAE Trans. **82**, 1287–1306 (1973).

[17]M. Herr, K.-S. Rossignol, J. Delfs, N. Lippitz, and M. Mößner, "Specification of porous materials for low-noise trailing-edge applications," in *Proceedings of 20th AIAA/CEAS Aeroacoustics Conference* (American Institute of Aeronautics and Astronautics, 2014).

[18]J. Delfs, B. Faßmann, N. Lippitz, M. Lummer, M. Mößner, L. Müller, K. Rurkowska, and S. Uphoff, "Sfb 880: Aeroacoustic research for low noise take-off and landing," CEAS Aeronaut. J. **5**, 403–417 (2014).

[19]A. Rubio Carpio, F. Avallone, D. Ragni, M. Snellen, and S. van der Zwaag, "Mechanisms of broadband noise generation on metal foam edges," Phys. Fluids **31**, 105110 (2019).

[20]S. A. S. Ali, M. Azarpeyvand, and C. R. I. da Silva, "Trailing-edge flow and noise control using porous treatments," J. Fluid Mech. **850**, 83–119 (2018).

[21]D. M. Freed, "Lattice-boltzmann method for macroscopic porous media modeling," Int. J. Mod. Phys. C **09**, 1491–1503 (1998).

[22]E. H. Dowell, C.-F. Chao, and D. B. Bliss, "Absorption material mounted on a moving wall-fluid/wall boundary condition," J. Acoust. Soc. Am. **70**, 244–245 (1981).

[23]C. K. Tam and L. Auriault, "Time-domain impedance boundary conditions for computational aeroacoustics," AIAA J. **34**, 917–923 (1996).

[24]S. R. Koh, M. Meinke, and W. Schröder, "Numerical analysis of the impact of permeability on trailing edge noise," J. Sound Vib. **421**, 348–376 (2018).

[25]H. Chen, S. Chen, and W. H. Matthaeus, "Recovery of the navier-stokes equations using a lattice-gas Boltzmann method," Phys. Rev. A **45**, R5339 (1992).

[26]V. Yakhot and S. A. Orszag, "Renormalization group analysis of turbulence. i. Basic theory," J. Sci. Comput. **1**, 3–51 (1986).

[27]J. E. Ffowcs Williams and D. L. Hawkings, "Sound generation by turbulence and surfaces in arbitrary motion," Philos. Trans. R. Soc., A **264**, 321–342 (1969).

[28]D. Casalino, "An advanced time approach for acoustic analogy predictions," J. Sound Vib. **261**, 583–612 (2003).

[29]F. Farassat and G. P. Succi, "A review of propeller discrete frequency noise prediction technology with emphasis on two current methods for time domain calculations," J. Sound Vib. **71**, 399–419 (1980).

[30]C. Sun, F. Pérot, R. Zhang, P.-T. Lew, A. Mann, V. Gupta, D. M. Freed, I. Staroselsky, and H. Chen, "Lattice Boltzmann formulation for flows with acoustic porous media," C. R. Méc. **343**, 533–544 (2015).

[31]E. Baril, A. Mostafid, L.-P. Lefebvre, and M. Medraj, "Experimental demonstration of entrance/exit effects on the permeability measurements of porous materials," Adv. Eng. Mater. **10**, 889–894 (2008).

[32]N. Dukhan and C. Minjeur, "Minimum thickness for open-cell metal foam to behave as a porous medium," in Proceedings of 40th Fluid Dynamics Conference and Exhibit (2010), p. 4618.

[33]C. Naaktgeboren, P. Krueger, and J. Lage, "Limitations of Darcy's law in light of inlet and exit pressure drops," in Proceedings of International Conference on Applications of Porous Media (2004).

[34]G. Elsinga and J. Westerweel, "Tomographic-PIV measurement of the flow around a zigzag boundary layer trip," Exp. Fluids **52**, 865–876 (2012).

[35]R. K. Amiet, "Noise due to turbulent flow past a trailing edge," J. Sound Vib. **47**, 387–393 (1976).

[36]T. F. Brooks, D. S. Pope, and M. A. Marcolini, "Airfoil self-noise and prediction," Report No. NASA-RP-1218, NASA Reference Publication, 1989.

[37]Q. Ye, F. Avallone, D. Ragni, M. M. Choudhari, and D. Casalino, "Effect of surface roughness on boundary layer transition and far field noise," in Proceedings of 25th AIAA/CEAS Aeroacoustics Conference (2019), p. 2551.

[38]J. F. Williams and L. Hall, "Aerodynamic sound generation by turbulent flow in the vicinity of a scattering half plane," J. Fluid Mech. **40**, 657–670 (1970).

[39]J. W. Jaworski and N. Peake, "Aerodynamic noise from a poroelastic edge with implications for the silent flight of owls," J. Fluid Mech. **723**, 456 (2013).

[40]A. Cavalieri, W. Wolf, and J. Jaworski, "Numerical solution of acoustic scattering by finite perforated elastic plates," Proc. R. Soc. A **472**, 20150767 (2016).

[41]M. Roger and S. Moreau, "Back-scattering correction and further extensions of Amiet's trailing-edge noise model. Part 1: Theory," J. Sound Vib. **286**, 477–506 (2005).

[42]W. van der Velden, A. van Zuijlen, A. de Jong, and D. Ragni, "Flow and self-noise around bypass transition strips," Noise Control Eng. J. **65**, 434–445 (2017).

[43]M. Howe, "The role of surface shear stress fluctuations in the generation of boundary layer noise," J. Sound Vib. **65**, 159–164 (1979).

[44]M. S. Howe, "A review of the theory of trailing edge noise," J. Sound Vib. **61**, 437–465 (1978).

[45]P. R. Spalart, "On the precise implications of acoustic analogies for aerodynamic noise at low Mach numbers," J. Sound Vib. **332**, 2808–2815 (2013).

[46]A. Kisil and L. J. Ayton, "Aerodynamic noise from rigid trailing edges with finite porous extensions," J. Fluid Mech. **836**, 117–144 (2018).

[47]J. Jeong and F. Hussain, "On the identification of a vortex," J. Fluid Mech. **285**, 69–94 (1995).

[48]J.-H. Lee and H. J. Sung, "Effects of an adverse pressure gradient on a turbulent boundary layer," Int. J. Heat Fluid Flow **29**, 568–578 (2008).

[49]Y. Kuwata and K. Suga, "Direct numerical simulation of turbulence over anisotropic porous media," J. Fluid Mech. **831**, 41–71 (2017).
[50]W. K. Blake, "Turbulent boundary-layer wall-pressure fluctuations on smooth and rough walls," J. Fluid Mech. **44**, 637–660 (1970).
[51]N. Hu, N. Reiche, and R. Ewert, "Simulation of turbulent boundary layer wall pressure fluctuations via Poisson equation and synthetic turbulence," J. Fluid Mech. **826**, 421–454 (2017).
[52]W. Breugem and B. Boersma, "The turbulent flow over a permeable wall," in *Proceedings of the Summer Program 2002* (Center for Turbulence Research, 2002), pp. 215–228.
[53]N. Curle, "The influence of solid boundaries upon aerodynamic sound," Proc. R. Soc. London, Ser. A **231**, 505–514 (1955).
[54]M. S. Howe, "Noise produced by a sawtooth trailing edge," J. Acoust. Soc. Am. **90**, 482–487 (1991).
[55]D. Palumbo, "Determining correlation and coherence lengths in turbulent boundary layer flight data," J. Sound Vib. **331**, 3721–3737 (2012).
[56]W. Van der Velden, A. Van Zuijlen, A. De Jong, and H. Bijl, "On the estimation of spanwise pressure coherence of a turbulent boundary layer over a flat plate," in *Proceedings-WCCM XI: 11th World Congress on Computational Mechanics; ECCM V: 5th European Conference on Computational Mechanics; ECFD VI: 6th European Conference on Computational Fluid Dynamics*, Barcelona, Spain, *20–25 July 2014* (CIMNE, 2014).
[57]D. E. Faleiros, M. Tuinstra, and H. Hoeijmakers, "Drag, lift and effective angle of attack from analysis wake of an airfoil in open-jet wind tunnel," in *Proceedings of 54th AIAA Aerospace Sciences Meeting 2016, San Diego, California, USA, 4–8 January 2016* (American Institute of Aeronautics and Astronautics, Inc., AIAA, 2016).